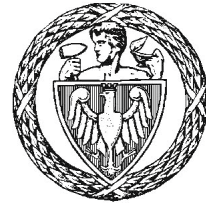


Warsaw University of Technology

Faculty of
Power and Aeronautical Engineering



Institute of Heat Engineering

Master's diploma thesis

in the field of study Power Engineering

Computational Modelling of Eutectic Metal Alloy Mg-51%Zn for Thermal
Energy Storage Using the Enthalpy Method

Thatchanon Samerpop

Student number 336300

thesis supervisor
Dr. Hab. Eng. Mirosław Seredyński

WARSAW 2025

Abstract

This study presents a computational fluid dynamics (CFD) investigation of a eutectic Mg-Zn alloy-based latent heat thermal energy storage (TES) system. A two-dimensional axisymmetric model was developed in ANSYS Fluent, using the enthalpy method to simulate the melting and solidification behavior of the phase change material (PCM), utilizing heat transfer fluid (HTF) as the heat source. The model incorporated temperature-dependent thermophysical properties, turbulence modeling by the $k-\omega$ SST approach, and transient heat transfer to capture the dynamics of both cycles.

The simulation results show that the melting of PCM initiates at the inner surface and progresses radially outward, driven by conduction and natural convection. In contrast, during solidification, a reversed thermal occurs, with the same heat transfer mechanism. The model predicts slightly longer durations than experimental data due to simplifications in boundary conditions and geometry. Validation against experimental data demonstrates good agreement in the temperature profile and phase change durations, with a deviation of approximately 5%. Moreover, the simulation provides a good observation of the evolution of relevant thermophysical parameters during these two phases.

A parametric study is also explored to investigate the effects of HTF flow direction and inlet velocity. It highlights the significance of fluid behavior, especially the turbulence regime, on heat exchange between two domains. The analysis confirms the critical role of dynamic flow in optimizing TES and further system improvement.

Overall, the results underscore the importance of incorporating both conduction and convection mechanisms in PCM modeling and offer practical insights for the design and optimization of latent heat TES systems. Recommendations for future work include an improved geometric simulation model and expanded material studies to assess system adaptability to other advanced materials in various fields.

Content

| | | |
|------|--|----|
| 1. | Introduction | 3 |
| 1.1. | Background | 3 |
| 1.2. | Problem Statement..... | 3 |
| 2. | Literature Review and Theoretical Framework..... | 4 |
| 2.1. | Thermal Energy Storage Systems in Renewable Energy..... | 4 |
| 2.2. | Overview of Molten Salt and Metallic Alloy Phase Change Materials..... | 5 |
| 2.3. | Computational Modeling in Thermal Systems | 8 |
| 3. | Methodology | 11 |
| 3.1. | Experimental Validation Setup..... | 11 |
| 3.2. | Materials Properties of the Thermal Energy Storage Unit | 12 |
| 3.3. | Experiment Procedure and Data Acquisition | 15 |
| 3.4. | Computational Model | 17 |
| 4. | Results | 21 |
| 4.1. | Model Validation | 21 |
| 4.2. | Simulation Result | 22 |
| 5. | Implications of the Simulation Model..... | 32 |
| 5.1. | Impact of HTF Flow Direction | 32 |
| 5.2. | Impact of HTF Flow Inlet Velocity | 33 |
| 6. | Conclusion and Discussion | 38 |
| | References..... | 40 |

1. Introduction

1.1. Background

Thermal energy storage (TES) systems are integral to enhancing the reliability and efficiency of renewable energy sources, particularly solar power. By storing excess thermal energy during periods of high availability, TES systems enable a more stable and continuous energy supply, mitigating the inconsistent nature of solar energy. These systems are especially critical in Concentrated Solar Power (CSP) plants, where they extend operational hours and ensure a stable electricity supply without relying on fossil fuel backup. This makes TES a vital technology in advancing renewable energy adoption [1].

Among the various TES technologies, latent heat storage using phase change materials (PCMs) stands out for its ability to store and release large amounts of energy during phase transitions. PCMs, such as molten salts and metallic alloys, maintain a relatively constant temperature during the phase change, making them highly efficient for applications requiring stable thermal storage. While molten salts are widely used due to their high thermal stability and cost-effectiveness, they are limited by low thermal conductivity and instability at elevated temperatures [2,3,4,5,6]. To address these limitations, metallic alloys have emerged as a promising alternative for high-temperature TES systems. Eutectic alloys, composed of elements such as aluminum, magnesium, and zinc, offer higher thermal conductivity and energy storage density compared to molten salts. Despite these advantages, research on metallic alloys for TES applications remains limited, particularly in understanding their behavior during phase transitions and optimizing their use in practical systems [4,7,8].

Computational modeling plays a crucial role in advancing the study of metallic alloys for TES. Numerical methods, such as the enthalpy method, enable detailed simulation of the heat transfer and phase change processes during alloy solidification and melting. These simulations provide valuable insights into the thermal behavior of eutectic alloys and inform the design of efficient TES systems [9,10]. Computational Fluid Dynamics (CFD) is one of the promising tools for simulating the alloy's phase transformation processes. This research utilizes this tool to investigate latent heat TES systems using metallic alloys PCMs [11,12].

1.2. Problem Statement

Despite the promising thermal properties of metallic eutectic alloys, research on their application in TES still needs to be advanced, particularly in the computational modeling of phase-change dynamics. While metallic alloys gain the advantage of higher thermal conductivity, their melting and solidification behavior, especially concerning convective heat transfer within the liquid phase, is poorly understood. This study aims to investigate how conduction dominates heat transfer and quantify the role of convection in accelerating or impeding phase transitions. Moreover, the enthalpy method in CFD is employed to model the melting and solidification behavior of Mg-Zn eutectic alloys. By validating simulation results against experimental data, the study expects to refine numerical approaches for predicting phase-change behavior in metallic PCMs. Lastly, the parametric study can be carried out using the successfully validated model for further understanding and optimization of TES.

2. Literature Review and Theoretical Framework

2.1. Thermal Energy Storage Systems in Renewable Energy

The utilization of solar energy as a renewable energy system (RES) has recently been widely implemented, with photovoltaic (PV) and CSP as compromising technologies. PV directly converts sunlight into electric energy, making it efficient to use. However, one of the challenges with PV systems is the mismatch between generation and demand; as sunlight duration is limited, CSP is taken into consideration. Unlike PV, CSP focuses on converting sunlight to generate heat, which can be stored thermally. This heat can then be converted into electricity when needed, offering a more stable power output [1].

TES is the component of the system that plays a critical role in enhancing the reliability of CSP by capturing solar energy during peak sunlight hours and discharging it during periods of low sunlight or nighttime, resulting in improved performance of solar thermal plants. This makes TES a vital technology in renewable energy systems, particularly in CSP plants, where stored energy is crucial for consistent electricity generation without fossil fuel backup [1].

Several key parameters can characterize TES. Firstly, capacity refers to the amount of energy that can be stored and is influenced by the storage medium, system size, and process type. Power indicates the rate at which energy can be charged or discharged, and efficiency measures how much of the input energy is retrievable for use. Additionally, the storage period defines how long energy can be retained, while charge/discharge time relates to the duration needed to load or unload the system. Lastly, the cost of TES is commonly expressed in €/kWh or €/kW, factoring in both capital investment and lifespan [13].

Various approaches are studied to enhance the TES system's cost-effectiveness and efficiency based on its characterization, as shown in Figure 2.1. Prieto et al. [15] introduced the use of thermochemical, including sulfur-based metal oxide cycles, with approximately 432-900 kJ/kg and 75-100% in capacity and efficiency, respectively. While sensible heat storage (SHS), known as the most uncomplicated storage, uses the benefit of change in temperature of a solid or liquid medium, its capacity is the least, around 36-180 kJ/kg [13,16]. TES systems with Phase Change Materials (PCMs) are promising methods for utilizing latent heat. They efficiently store and release large amounts of latent heat during phase transitions between solid and liquid states. PCMs maintain a relatively constant temperature during the phase change, making them ideal for solar thermal systems where stable thermal storage is needed. This ability allows for the increase of overall storage capacity performance and cost effectiveness using PCMs compared to sensible heat materials. PCMs, such as molten salts and metallic alloys, provide higher energy densities and make them suitable for high-energy applications. The latent heat of fusion in these materials, ranging from 172 kJ/kg to 400 kJ/kg, allows TES systems to absorb and release heat efficiently, improving the performance of CSP plants [2]. Regarding storage period and cost, while the chemical reaction TES system offers higher capacity and efficiency, it can deliver at most for daily durations and costs up to 100 €/kWh. In contrast, sensible and latent systems can operate with a wider range, from hourly to monthly, depending on their application, with less than 50 €/kWh [1].

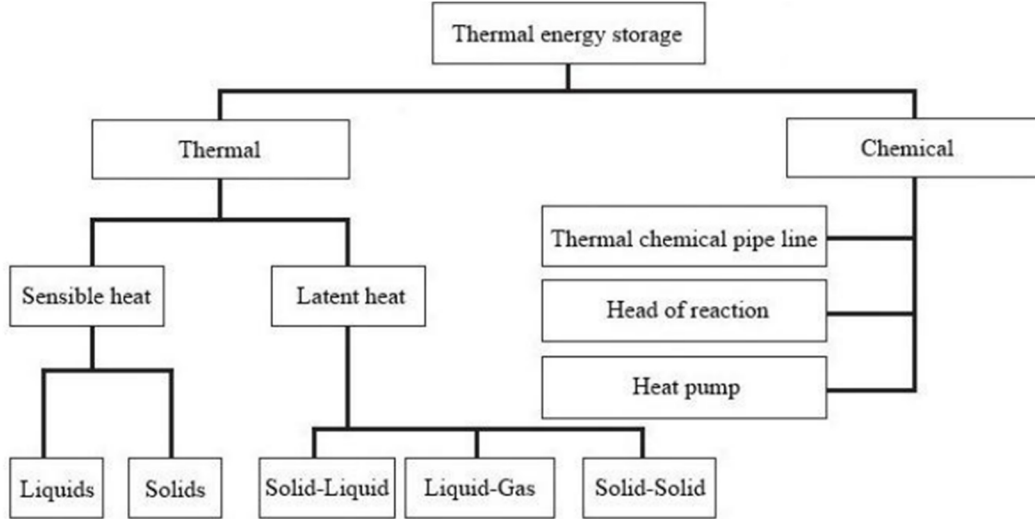


Figure 2.1. Characterization of solar TES [1].

2.2. Overview of Molten Salt and Metallic Alloy Phase Change Materials

Molten salt PCMs are widely used in CSP systems due to their high thermal stability and cost-effectiveness. They are ideal for TES systems because of their ability to operate in a wide range of temperatures up to 832°C, depending on their composition. For example, molten salts with chloride and carbonate composition are commonly used because of their affordability and ability to store heat [3,4]. However, these salts are limited by their low thermal conductivity, depending on temperature, at less than 1 W/mK, reducing heat transfer efficiency [5]. Additionally, molten salt PCMs tend to be unstable at high temperatures. Araki et al. [6] conducted an extensive investigation into the thermophysical properties of alkaline carbonate salts, representing eutectic compositions with melting points at 408-505°C. These compositions demonstrate instability at higher temperatures beyond their melting points because they begin to degrade when temperatures exceed these limits, affecting their long-term stability and thermal performance in high-temperature applications.

According to the limitations of molten salt PCMs, metallic alloy is considered in high-temperature TES systems, which can perform in applications where the temperature often exceeds 900°C. One significant advantage of metallic alloys is their higher thermal conductivity compared to molten salts, which allows for more efficient and faster heat transfer during phase transitions, reducing the time needed for energy charging and discharging. Additionally, metallic alloys exhibit greater energy storage density, meaning they can store more energy per unit volume, which is beneficial for compact systems. However, it is not broadly studied for the latent heat TES application, which provides a gap in research [4, 8].

Among metallic elements, Al, Cu, Mg, Si, and Zn are frequently implemented in binary and ternary eutectic alloys because of their high heat of fusion, as shown in Figure 2.2. Farkas and Birchenall [7] carried out the experiment on the eutectic alloy with the mentioned metal composition and reported the thermophysical properties in Table 2.1. The result shows their wide range of melting temperatures and heat of fusion, making them significant candidates for various purposes. Furthermore, most studies focused on relatively low-cost alloys such as Al-Si, Mg-Zn,

and Al-Mg-Zn alloys, as they can perform in high-temperature ranges and have suitable thermophysical properties [8]. Therefore, some advancements in these eutectic alloys will be presented.

Table 2.1 Thermophysical properties of some alloys [4]

| Composition (wt.%) | T _m [°C] | ΔH _f [J/g] | ρ [g/cm ³] | C _{ps} [J/g·K] | C _{pl} [J/g·K] |
|----------------------|---------------------|-----------------------|------------------------|-------------------------|-------------------------|
| Zn(52)-48Mg | 340 | 180 | | | |
| Al(59)-35Mg-6Zn | 443 | 310 | 2.38 | 1.63 | 1.46 |
| Mg(60)-25Cu-15Zn | 452 | 254 | 2.8 | | |
| Mg(52)-25Cu-23Ca | 453 | 184 | 2 | | |
| Al(54)-22Cu-18Mg-6Zn | 520 | 305 | 3.14 | 1.51 | 1.13 |
| Al(65)-30Cu-5Si | 571 | 422 | 2.73 | 1.3 | 1.2 |
| Zn ₂ Mg | 588 | 230 | | | |
| Zn(49)-45Cu-6Mg | 703 | 176 | 8.67 | 0.42 | |
| Cu(91)-9P | 715 | 134 | 5.6 | | |
| Cu(69)-17Zn-14P | 720 | 368 | 7 | | |
| Cu(74)-19Zn-7Si | 765 | 125 | 7.17 | | |
| Cu(56)-27Si-17Mg | 770 | 420 | 4.15 | 0.75 | |
| Mg(84)-16Ca | 790 | 272 | 1.38 | | |
| Mg(47)-38Si-15Zn | 800 | 314 | | | |
| Cu(80)-20Si | 803 | 197 | 6.6 | 0.5 | |
| Cu(83)-10P-7Si | 840 | 92 | 6.88 | | |

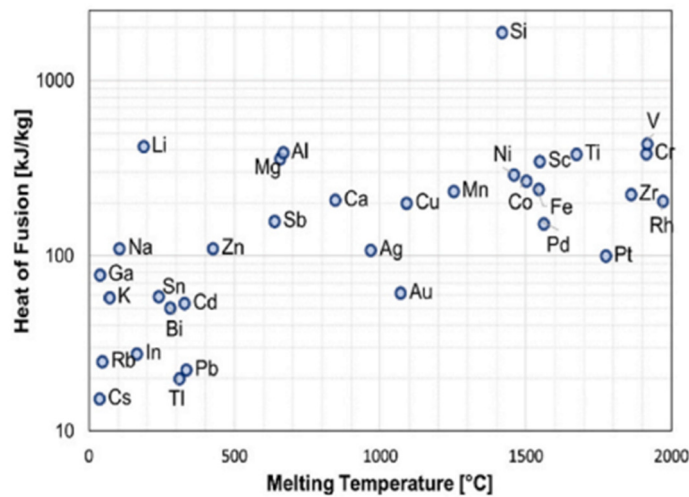


Figure 2.2. Heat of Fusion of metallic elements [8].

Al-Si is a simple eutectic system with two solid solution phases. Its eutectic temperature is around $577 \pm 1^\circ\text{C}$, and its eutectic composition is 12.2%, as shown in Figure 2.3 [17]. Wang et al. [18] used DCS (differential scanning calorimeter) method to investigate two composition alloys of aluminum and silicon, AlSi₁₂, which stand out with melting points at 576°C, confirming the eutectic temperature of previous literature. This alloy also demonstrates significantly higher thermal conductivity, typically at 160 W/mK, which enhances the heat transfer rate. Additionally, the paper compared the average heat discharge rate with Fe₃O₄ sensible heat storage from the

experiment, resulting in a figure better than 1.5 times in Figure 2.4, ensuring faster heat availability when needed. Furthermore, Kotzé et al. [14] conducted an experiment with AlSi₁₂ alloy to evaluate its behavior in TES in a steam generator application. The research aimed to measure heat transfer rates and track phase change behavior during heating and cooling cycles. The result showed the feasible safe design of AlSi₁₂-based TES-unit and its competitiveness when compared with molten salt.

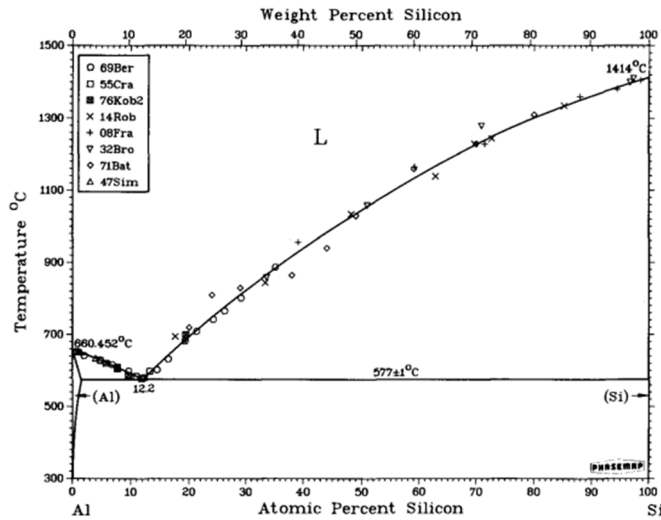


Figure 2.3. Al-Si phase diagram [17].

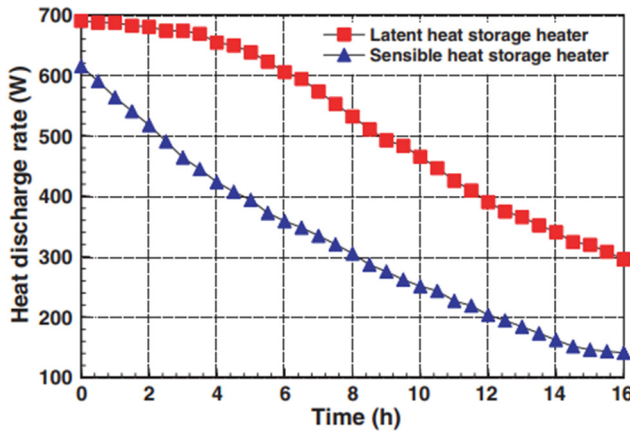


Figure 2.4. Comparison of the heat discharge rate of latent (AlSi₁₂) and sensible (Fe₃O₄) heat storage heaters from experimental results [18].

Other potential eutectic alloy candidates for latent heat TES were intensively investigated by the CIC Energigune laboratory. Blanco-Rodríguez et al. [19] carried out an experiment on the Mg-Zn eutectic alloy (Mg-51%Zn), which involved a unit composed of two concentric cylinders set up where the alloy was placed in the annular space between the cylinders. A synthetic oil heat transfer fluid (HTF) flows through the inner pipe, exchanging heat with the surrounding alloy during charging (melting) and discharging (solidification) cycles. It reported quasi-constant melting and solidification temperatures at 342°C and high thermal conductivity, with values of 75 W/mK in the solid phase and 35 W/mK in the liquid phase. Risueno et al. [20] experiment on Al-

Mg-Zn three ternary alloys, which are $\text{Mg}_{71}\text{Zn}_{28.9}\text{Al}_{0.1}$ and $\text{Mg}_{70}\text{Zn}_{24.4}\text{Al}_{5.6}$, quasi-peritectic alloys, whereas $\text{Mg}_{70}\text{Zn}_{24.9}\text{Al}_{5.1}$ is a eutectic alloy. This research uses various methods to characterize the microstructure during solidification in the synthesis process. Some significant thermophysical properties were also reported, and it was concluded that the eutectic alloy is the best candidate aside from the quasi-peritectic alloy for TES applications due to long-term stability under the phase transition process. Additionally, some other alloys, for example, Al-Si-Sb, Mg-Si-Zn, etc., which are considered cost-effective and suitable for such applications, should be performed.

2.3. Computational Modeling in Thermal Systems

Computational modeling can utilize numerical methods to simulate the fluid's behavior. It plays a crucial role in studying PCMs, especially eutectic alloys, by allowing researchers to simulate and analyze the complex heat transfer and phase change processes during melting and solidification. These simulations provide valuable insights into the thermal behavior of PCMs under different operational conditions, such as varying heat fluxes, cooling rates, and material properties. For eutectic alloys, numerical modeling clarifies critical factors such as lamellae growth in a diffusive environment and diffusive-convective heat transfer phenomena. Additionally, it can simulate and predict solidification patterns and their influence on the thermal performance of TES systems. This is particularly important for optimizing the design and efficiency of thermal energy storage systems where eutectic alloys are used. However, there are some challenges in applying the computational eutectic model due to the multi-phase simulation, and it is computationally intensive if an extremely fine grid is needed to capture the precise interfacial region. Therefore, many methods have been considered to investigate its behavior [9].

The phase-field method is introduced, and its basic concept is to avoid tracking sharp phase boundaries by solving additional equations for phase-field functions. It relies on a thermodynamically consistent phenomenologically free energy and allows a binary eutectic alloy solidification model to govern the Navier-Stokes and transport equations. However, it is limited by the extremely fine grid needed, the high number of Rayleigh cases, and the fact that it can be used in just microscale analysis [21]. The enthalpy method is one of the compromise methods and is widely used. This technique uses the latent heat at each node in the computational domain to follow the solidification interface. It is governed by the energy equation and temperature-solid fraction dependent coupling, allowing the solidification process to be modeled. The enthalpy method has been applied to macro-scale solidification of pure metals and alloys, and more recently, it has been adapted for dendritic solidification at the micro-scale [9].

The enthalpy method is broadly implemented in micro- and macro-scale analysis of eutectic alloys. Bhattacharya et al. [9] researched simulated regular eutectic solidification on a micro-scale, providing a generalized framework for studying complex eutectic systems and validating the model with theoretical benchmarks. Considering a larger system, macro-scale analysis using this method is also broadly investigated. Gnauk et al. [10] used the generalized enthalpy method to model heat and mass transport in multi-phase systems of Ti-Al at the macro level, particularly on the millimeter scale. Enthalpy is utilized as a critical parameter to calculate energy flow and simplify the simulations. This method is computationally efficient and suitable for simulating complex material systems, including those with different intermetallic phases of Ti-Al components.

As discussed, the enthalpy method reformulates the phase change problem by eliminating the need to track the solid-liquid boundary. Instead, a single set of equations is applied across the entire domain, allowing for a fixed mesh approach where the interface emerges implicitly. This method uses enthalpy as a primary variable and temperature as a secondary variable, creating a mushy region at the solid-liquid interface, which creates a smooth transition and prevents numerical instability. This relationship between enthalpy and temperature is usually assumed to be a step function for isothermal phase change problems, as shown in [Figure 2.5](#). As a result, the method handles phase change problems more effectively when undergoing melting or solidification [11,22].

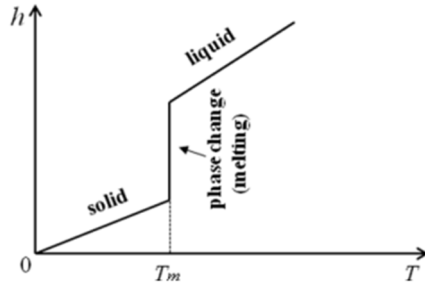


Figure 2.5. Relationships between enthalpy and temperature for isothermal phase change [12].

In computational modeling tools, like Computational Fluid Dynamics (CFD), the enthalpy method is often used to model PCMs in various applications. This integration allows for a continuous solution across liquid and solid phases, accurately capturing heat transfer and phase change dynamics in the thermal system. It allows the energy governing equation, which comprises the transient heat mechanism, the diffusive-convective term, and heat generation from other sources, to be solved iteratively. In the application, where the complexity of the phase change process, typically in eutectic alloy systems, is evaluated, the use of CFD becomes vital. CFD with the enthalpy method allows for the simulation of heat and mass transfer during alloy solidification on a larger scale when a fixed-grid control volume approach is used. It integrates heat, mass, and solute transport in the entire domain without explicitly tracking the solid-liquid boundary. CFD provides a robust framework to incorporate solute convection, temperature gradients, and solute diffusion within the alloy's mushy region [12,22].

Implementing this fluid dynamic simulation as a tool for the utilization of PCMs in TES applications has proven the efficiency and accuracy of CFD in many studies. Shukla and Kishan [33] implemented CFD to simulate the melting behavior of PCM in a shell-and-tube latent heat TES system. Using a transient two-dimensional model and the enthalpy-porosity method, the study captures the coupled heat transfer and natural convection effects during phase transition. Even though the study didn't include eutectic alloy as PCMs, the simulation demonstrated good agreement with experimental data and confirmed CFD as an accurate and efficient tool for analyzing PCM behavior for TES designs.

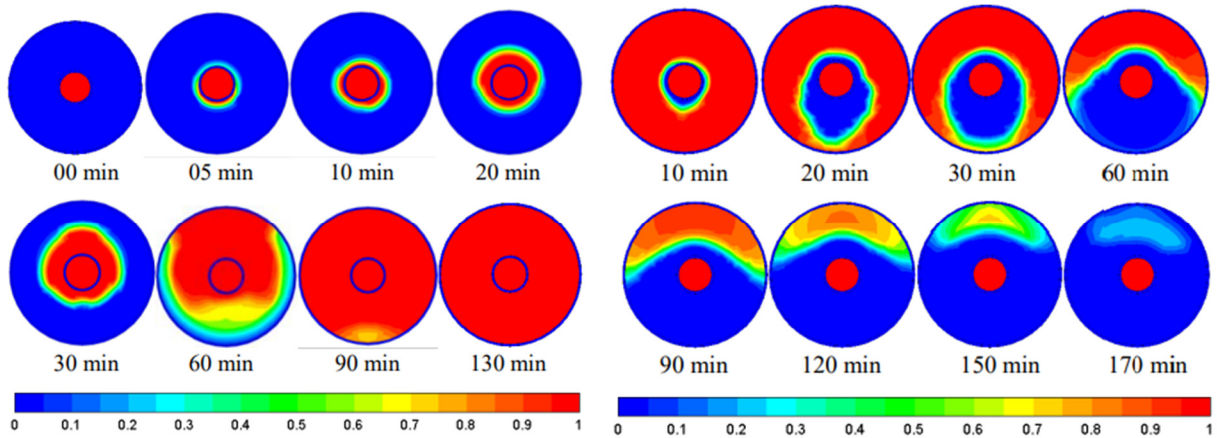


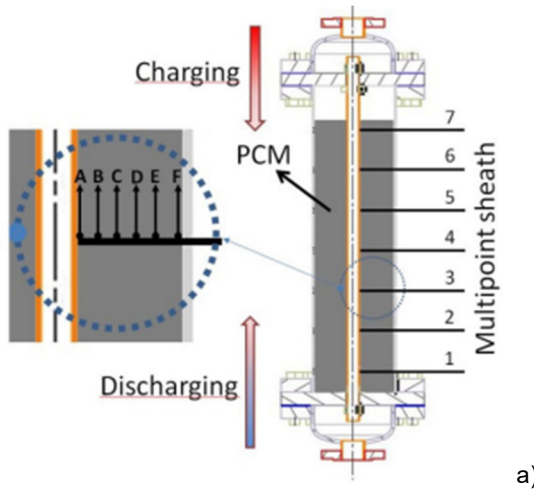
Figure 2.6. Liquid fraction contour as a result of CFD simulation for the charge and discharge process of PCM in the TES system [33].

3. Methodology

3.1. Experimental Validation Setup

The computational model uses the following experimental setup, which consists of a TES unit using a Mg-51 % Zn eutectic alloy as PCM for validation. The unit is designed with concentric cylinders, enclosing PCM within an annular space. The one-inch diameter inner and eight-inch diameter outer steel cylinders act as heat transfer surfaces, facilitating the charging (melting) and discharging (solidification) processes [19].

Key components of the setup include an oil test loop and a TES unit. In the oil test loop, SYLTERM 800 is used as heat transfer fluid (HTF), with a magnetic circular pump, electrical heaters, and an air fan heat exchanger as the components to operate the loop. For the TES unit, SS304 steel is used as the cylinder's material to contain Mg-51%Zn based on a compatible and economic basis. HTF flows through the inner pipe with 1 m/s velocity surrounded by eutectic alloy. While it flows from the top and exits at the bottom of the unit during the charging process, the flow is reversed during the discharging process. Moreover, to observe temperature, seven multipoint sheaths are placed along the axial direction with six K-type thermocouples on each sheet in the radial direction, and the details of the model's dimensions are displayed in Figure 3.1. Additionally, the figure also shows six thermocouples on the sheath four, which will be used to validate the simulation result, specifically thermocouple 4A to 4F as T 4A to T 4F. However, as the description regarding model dimensions in the literature is unclear, the dimension of this simulation is defined by available physical and geometry data. The position of sheathes and thermocouples is also based on the assumption that they are placed evenly along both directions.



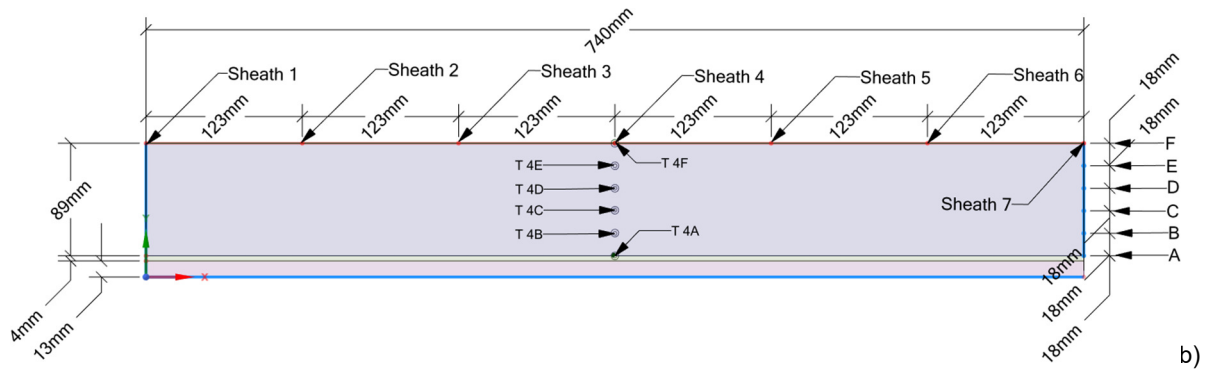


Figure 3.1. a) Schematic diagram of the TES unit with the thermocouples distributed on the sheaths [19]. b) Dimension of the simulation model with metal sheaths and thermocouples position.

3.2. Materials Properties of the Thermal Energy Storage Unit

The TES unit is the component where heat transfer occurs. Therefore, it is crucial to identify the material properties of the eutectic alloy, steel, and HTF to observe the melting and solidification process.

3.2.1. Mg-51%Zn eutectic alloy

The eutectic alloy magnesium 49% wt. and zinc 51% wt. is used because of its favorable thermophysical properties, and it has already been proposed as a PCM for TES. Figure 3.2. illustrates the binary phase diagram of the Mg-Zn alloy system and the melting temperature at around 615 K. At this phase transition temperature, the melting and solidification enthalpies (L) are 155 J/g, defined by the DSC technique [23].

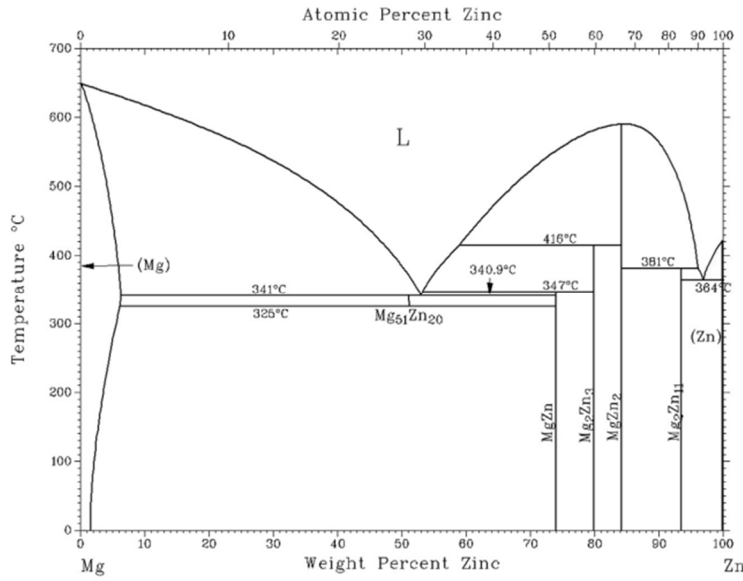


Figure 3.2. Binary phase diagram of Mg and Zn [23].

Specific heat (c_p) is an important thermodynamic property of the alloy and can also be investigated by the DSC experiment. After theoretical modeling based on phase transformations and enthalpy changes, Figure 3.3 shows the variation of c_p with temperature. Curve three exhibits

the contribution of harmonic, electronic, and Nernst–Lindemann anharmonic-specific heat. Moreover, a linear relation between heat capacity and temperature is observed beyond the room temperature. Therefore, the figure will be used to define the c_p value in modal [24].

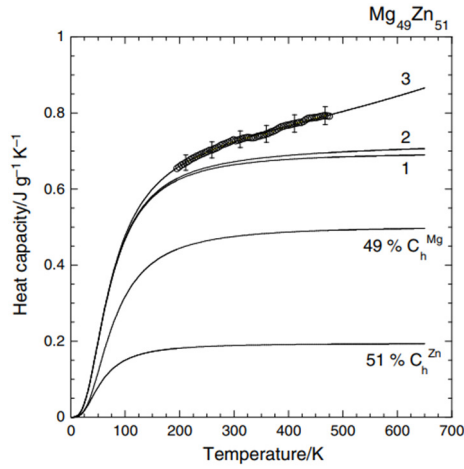


Figure 3.3. Result of determination of c_p value for Mg₄₉Zn₅₁ eutectic alloy [24].

Thermal conductivity (k) is also a vital parameter for studying eutectic alloys for TES applications, and it can be obtained from the following equation.

$$k = \alpha \rho c_p \quad (1)$$

Where α is thermal diffusivity [m^2/s], and ρ is density [kg/m^3].

Density is defined by various literature depending on the temperature and composition of Mg and Zn. In this study, the maximum density of alloys with perfect crystal lattices with no defects is implemented at 3440 kg/m³. Thermal diffusivity is a temperature-dependent parameter and can be obtained from experimental data. Figure 3.4 shows that the thermal diffusivity value of two different phases of Mg-Zn alloys varies with temperature [23].

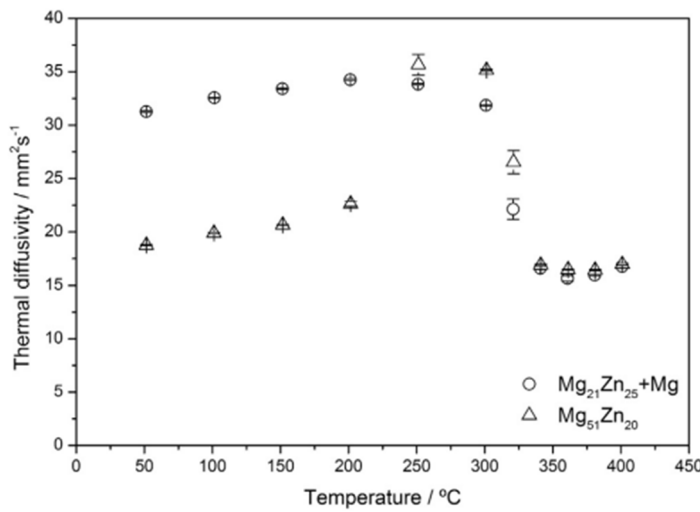


Figure 3.4. Thermal diffusivity of Mg₂₁Zn₂₅ + Mg and Mg₅₁Zn₂₀ alloys [23].

The thermal expansion coefficient (β) can be defined as follows.

$$a = \frac{V\beta^2}{c_p^2 k_T} \quad (2)$$

$$V = 1/\rho \quad (3)$$

Where k_T is isothermal compressibility [1/Pa], V is specific volume [m^3/kg], and a is an empirical parameter [g/J].

The empirical parameter is a nearly constant value over the temperature range and can be used to define c_p in case of an unknown expansion coefficient through empirical fitting. The empirical selection of $a = 3.4 \times 10^{-4}$ g/J for the thermodynamic study of Mg-Zn alloy is implemented. Isothermal compressibility can be estimated by the property of pure metal in the order of 10^{-11} [24,27].

One of the critical properties of modal melting alloy is viscosity, commonly estimated using empirical correlations, such as the Andrade-type equation shown in [Equation \(4\)](#). This widely used formula provides a quantitative correlation for the viscosity of pure liquid metals and alloys, particularly near their melting points. It demonstrates relationships between viscosity and other thermophysical properties, such as atomic number, melting temperature, surface energy, and molar volume. The formula captures the temperature dependence of viscosity based on the idea that the specific heats of solids and liquids near the melting point are significantly close, implying similar atomic vibrational behavior in both phases [28].

$$\mu(T_m) = C_A \frac{\sqrt{AT_m}}{V^{2/3}} \quad (4)$$

Where $\mu(T_m)$ is viscosity [$kg/m s$], C_A is an empirical constant [$(J/K mol^{1/3})^{1/2}$], A is atomic weight [g/mol], and V is molar volume [m^3/mol].

In modeling the viscosity of eutectic alloy, the Andrade-type correlation is modified, though its reliability varies depending on the nature of the eutectic. Based on various literature, the parameter C_A of eutectics line around $(1.85 \pm 0.4) \times 10^{-7}$ $(J/K mol^{1/3})^{1/2}$, close to those of pure metals. For Mg₄₉Zn₅₁ eutectic alloy $C_A = 2.2 \times 10^{-7}$ $(J/K mol^{1/3})^{1/2}$ is implemented, resulting in $\eta = 1.64 \times 10^{-3}$ kg/m s [28].

[Table 3.1](#) summarizes the thermophysical properties of Mg-Zn eutectic alloy based on experimental results from various literature.

Table 3.1 Thermophysical properties of Mg₄₉Zn₅₁ eutectic alloy

| Properties | Value |
|---------------------------------------|-----------------------|
| Melting Temperature [K] | 615 |
| Density [kg/m^3] | 2850 |
| Latent heat of fusion [J/kg] | 1.28×10^5 |
| Thermal expansion coefficient [1/K] | 1.35×10^{-4} |
| Specific heat of at 573 K [J/kg K] | 830 |
| Specific heat of at 663 K [J/kg K] | 870 |
| Thermal conductivity at 573 K [W/m K] | 78 |
| Thermal conductivity at 615 K [W/m K] | 41 |
| Viscosity [$kg/m s$] | 1.64×10^{-3} |

3.2.2. SS304 steel

SS304 was chosen as the TES unit's container material because of its compatibility with PCM properties and economic basis. [Table 3.2](#) demonstrates thermophysical properties that are compiled [19,25].

Table 3.2 Thermophysical properties of SS304 steel [25]

| Thermophysical properties | Value |
|---|-------|
| Specific heat of solid phase [J/kg K] | 700 |
| Thermal conductivity of solid phase [W/m K] | 22 |
| Density of solid phase [kg/m ³] | 7200 |

3.2.3. SYLTHERM 800 HTF

Silicone Heat Transfer Fluid, specifically SYLTHERM 800, is used to transfer energy between the oil loop and the TES unit because of its highly stable, high-temperature liquid phase operation and low toxicity properties. [Table 3.3](#) shows some essential properties of this HTF [19,26].

Table 3.3 Properties of SYLTHERM 800 HTF [26]

| Properties | Value |
|---------------------------------------|------------------------|
| Specific heat at 553 K [J/kg K] | 2052 |
| Specific heat at 673 K [J/kg K] | 2257 |
| Thermal conductivity at 553 K [W/m K] | 0.0861 |
| Thermal conductivity at 673 K [W/m K] | 0.0635 |
| Density at 553 K [kg/m ³] | 692.87 |
| Density at 673 K [kg/m ³] | 547.00 |
| Viscosity at 553 K [kg/ms] | 5.4 x 10 ⁻⁴ |
| Viscosity at 673 K [kg/ms] | 2.5 x 10 ⁻⁴ |

3.3. Experiment Procedure and Data Acquisition

The experiment follows a controlled thermal cycle to evaluate the heat transfer characteristics of the Mg-51 % Zn eutectic alloy TES unit. The procedure consists of charging and discharging phases as follows:

During the charging process, the oil inlet and eutectic alloy are initially set at 579 K. The preheating of the solid alloy starts where the oil's temperature linearly rises to approximately 654 K for a duration of about 1,200 seconds. The energy is then transferred to the alloy, and the temperature increases to the melting point at 615 K. At this point, the solid-to-liquid transition of the alloy can be observed. After fully melting, its temperature increases until it reaches a superheating state at the same temperature as the oil inlet.

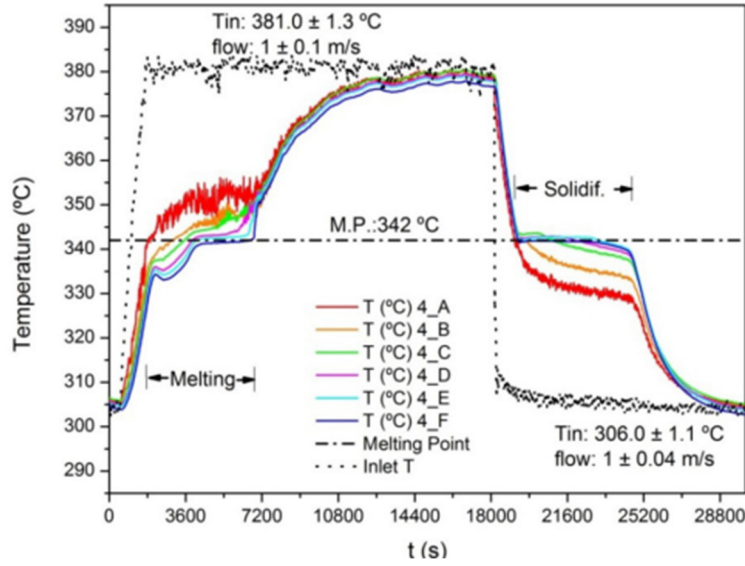


Figure 3.5. Temperature evolution during the melting and solidification processes of the eutectic alloy is measured by thermocouples of sheath 4 [19].

The same applies to the discharging process, but it is reversed. The temperature of the oil was set to 579 K to extract heat from the 654 K liquid PCM. When dropping to 615 K, the solidification of the alloy occurs. Then, after solidifying, the temperature continuously decreases to the same point as oil. Figure 3.5 demonstrates the temperature behavior of these heating and cooling processes at specific points of the eutectic alloy.

To analyze the system's thermal performance, data is continuously recorded and processed using several thermocouples placed on the sheaths, as stated in the experimental validation setup section. Figure 3.6 illustrates the temperature evolution of six thermocouples on sheaths in the melting and solidification process, which can be used for modal validation, as well as Figure 3.5.

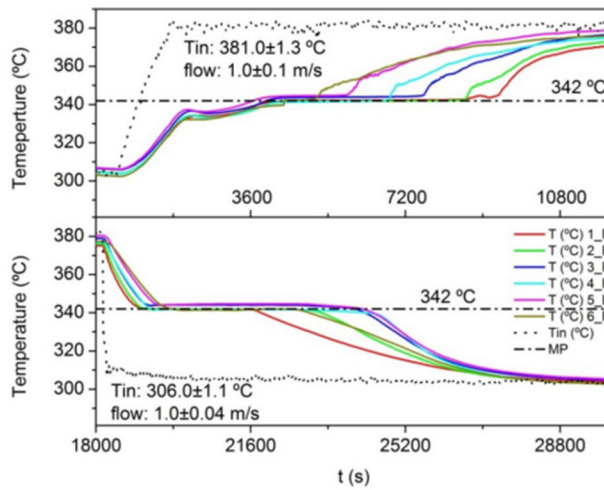


Figure 3.6. Temperature evolution during the melting and solidification processes of the eutectic alloy is measured by thermocouples F on all sheaths [19].

3.4. Computational Model

3.4.1. Physical Model

Understanding the physical behavior of eutectic alloy is mandatory to create the computational model. According to the binary phase diagram of Mg and Zn in [Figure 3.2](#), the liquidus and solidus boundaries and eutectic points can be identified.

The liquidus line is the temperature above which the material is entirely liquid. Below this line, solid phases start to form. In contrast, the solidus line is the temperature below which the material is completely solid, and some liquid phase may still exist above this line. The slopes of the liquidus and solidus lines describe how the onset temperatures of the phase change vary with solute concentration. At the liquidus slope, the temperature for solidification begins, while the solidus slope defines when the alloy is fully solid. The eutectic point is the unique composition and temperature at which the liquid phase is in thermodynamic equilibrium with two distinct solid phases, and during cooling, the liquid solidifies into both solids simultaneously. Regarding the Mg-Zn system, the eutectic composition occurs around 615 K, referred to as the melting temperature, with Mg₄₉Zn₅₁ phase formation. [\[17,23\]](#).

3.4.2. Mathematical Model

The computational model solves the governing mass, momentum, and energy conservation equations, adopting the enthalpy method to track the phase change interface. An enthalpy formulation incorporates the latent heat with melting and solidification into the energy equation, which will be discussed in this section. To begin with, some assumptions must be made to simplify the complexity due to transient, nonlinear, and moving boundaries at the solid-liquid interface of the model [\[29\]](#).

- Two-dimensional finite axisymmetric problem.
- Heat transfer and phase change in the eutectic region are affected by conduction and natural convection.
- The eutectic alloy is isotropic and homogeneous. The volume change is negligible during the melting and solidification process.
- Constant heat transfer fluid inlet temperature and velocity. This fluid is incompressible and Newtonian.
- The latent heat fusion is the only source of internal heat formation.

The system will be considered along with the positive x-axis, initially maintained at a constant oil inlet temperature. The direction of heat transfer will differ according to the charge and discharge state in [Section 3](#), so the gravity sign must be considered. The mushy zone (A_{mush}) is the amplitude of the damping between both phases, advances in the y-direction, the same as the heat transfer direction. A value of $A_{mush} = 10000$ is used, considered a proper value in this case. Conduction will dominate during the solid phase and the solidification process as a heat transfer mechanism, whereas conduction-convection occurs during the melting of PCM. However, heat convection might be limited because of the high thermal conductivity of PCM and small temperature change along both axes [\[19,29\]](#).

An energy balance equation, [equation 5](#), at the solid-liquid interface is essential to capture phase change behavior fully. The energy governing equation, modified to account for latent heat

effects using a source term based on a solid fraction, can be expressed as follows. Moreover, the enthalpy method is utilized to model the phase transition of PCM. It is known as the Solidification and Melting model in the FLUENT software package. Rather than explicitly tracking the liquid-solid interface, it employs an enthalpy-porosity formulation, where the solidified region is modeled as a porous medium. This method defines porosity by the liquid fraction within each computational cell and is updated at every iteration based on the enthalpy balance [19,30].

$$\frac{\partial(\rho c_p T)}{\partial t} = \nabla(k \nabla T) + \rho L \frac{\partial g_s(T)}{\partial t} \quad (5)$$

Where L is the latent heat of fusion, g_s is the alloy's solid fraction and is assumed to depend on the local temperature linearly, as in equation (6).

$$g_s = \begin{cases} 1 & \text{if } T < T_s \text{ (solid)} \\ \frac{T_l - T}{T_l - T_s} & \text{if } T_l < T < T_s \text{ (mushy)} \\ 0 & \text{if } T > T_l \text{ (liquid)} \end{cases} \quad (6)$$

Where T_l is the liquidus temperature of the alloy [K], and T_s is the solidus temperature of the alloy [K].

For eutectic alloys, the solid fraction transitions at the eutectic temperature as both the solidus and liquidus temperatures coincide. This results in an isothermal phase change with no mushy region, so it does not vary linearly with temperature but changes suddenly from 0 to 1.

The momentum sink (M_s) is introduced to show the melting/solidification process as follows [19].

$$M_s = \frac{(1 - g_l)^2}{(g_l^3 + \varepsilon)} A_{mush} (\vec{v} - \vec{v}_p) \quad (7)$$

Where g_l is the liquid volume fraction, ε is a small number to prevent division by zero, \vec{v} is the velocity of the liquid [m/s], and \vec{v}_p is the solid velocity due to the pulling velocity of solidified material out of the domain [m/s].

In this simulation, the pulling velocity is considered zero and cancel out, as solidification proceeds without external drive motion, and the front advances due to just thermal and concentration diffusion.

Lastly, convective heat transfer is the primary distribution mechanism for heat transfer. This domain consistently remained in a turbulent flow regime with $Re > 40000$. A standard k- ω SST Reynolds-Averaged Navier-Stokes (RANS) model is employed to model the fluid dynamics under these conditions. The model is a widely used RANS-based approach for simulating turbulent flows. It solves two transport equations: one for the turbulent kinetic energy (k) and one for the specific dissipation rate (ω), capturing turbulence energy and its dissipation rate. As a low-Reynolds-number model, it is well-suited for near-wall flow regions, accurately resolving the

viscous sublayer. It performs well in complex boundary layer conditions with adverse pressure gradients and flow separations, making it ideal for this application.

3.4.3. Geometry and Boundary Conditions

The domain of the model includes the HTF region (lower green mesh area), steel pipe (grey area), and the surrounding PCM region (upper green mesh area), as shown in [Figure 3.7a](#). Key boundary conditions corresponding to each region, including oil-steel and steel-alloy boundaries. Additionally, to make the model be able to represent the physical model, the mesh must be fine enough, but not too fine, to avoid limited computing power. Therefore, the number of divisions in the radial direction of oil, steel, and eutectic is 25, 4, and 90, respectively, and 600 divisions for all domains axially. Moreover, to effectively capture the heat transfer that occurs at the boundary, the mesh must be refined near the wall, as illustrated in [Figure 3.7b](#).

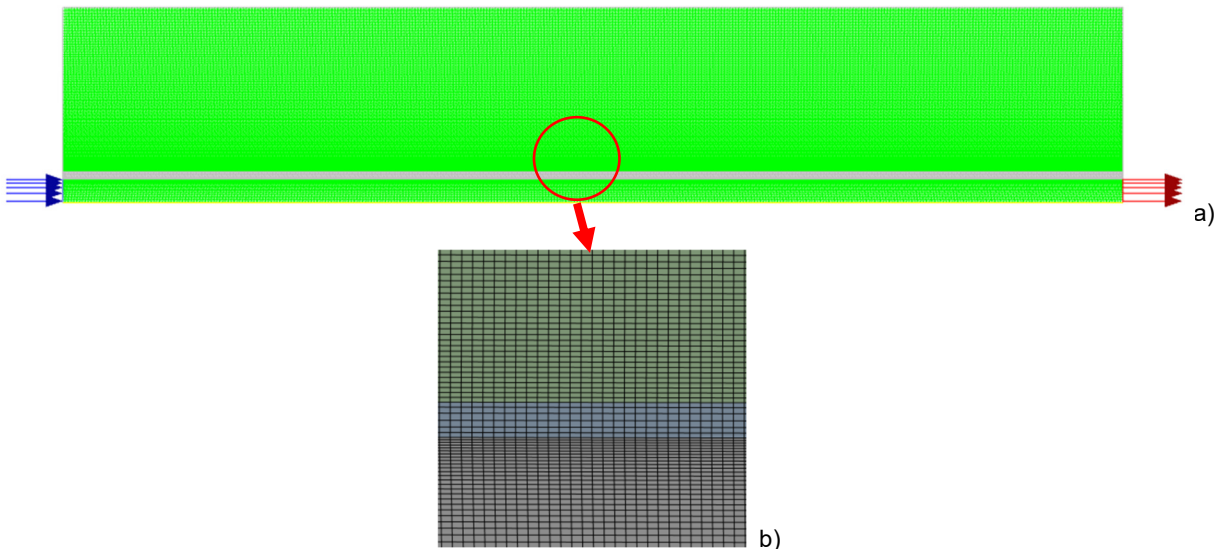


Figure 3.7. a) The schematic diagram represents the geometry and boundary conditions of the model. b) Mesh refinement near the oil.

The oil boundary conditions comprise fluid inlet (blue arrows) and outlet (red arrows), which assume a constant velocity inlet at 1 m/s. The lower boundary (yellow line) is the axisymmetric line of the model, and the upper one is the conductive heat transfer boundary to the steel region.

$$T_{oil}(x = 0, t) = 654 \text{ K}, t = [t_i, t_f] \text{ for charging process} \quad (8)$$

$$T_{oil}(x = 0, t) = 579 \text{ K}, t = [t_i, t_f] \text{ for discharging process} \quad (9)$$

For the SS304 steel region, the left and right side is adiabatic wall, while the top and bottom parts represent the contact line to the eutectic and oil areas, respectively.

The eutectic alloy domain is a major part of the study, where the upper, left, and right sides contact the insulator and are assumed to be adiabatic. The lower part allows heat transfer from the steel region to this area.

$$T_{eutectic,lower\ boundary}(t = 0) = 579 \text{ K for charging process} \quad (10)$$

$$T_{eutectic,lower\ boundary}(t = 0) = 654 \text{ K for discharging process} \quad (11)$$

3.4.4. Simulation Model

The numerical simulations were conducted using ANSYS Fluent, employing the finite volume method for spatial discretization. The PISO (Pressure-Implicit with Splitting of Operators) scheme is used for pressure-velocity coupling in CFD, which is particularly effective for transient simulations. It works by solving the momentum equations to predict velocity, followed by one or more pressure correction steps to enforce mass conservation and update the velocity field, as shown in [Figure 3.8](#). In the context of this study on eutectic alloy, which involves turbulent flow of HTF and phase change in the alloy, PISO is well-suited due to its ability to handle strong pressure-velocity coupling efficiently, offering improved stability and accuracy for transient heat transfer [31].

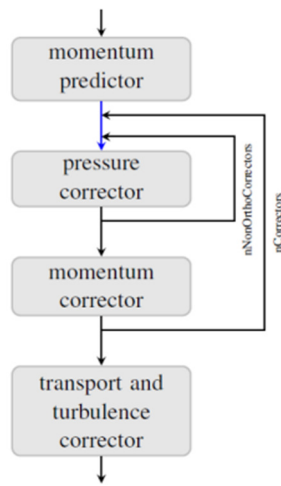


Figure 3.8. PISO algorithm [31].

The simulation directly models the flow of oil inside the pipe, which remained in the turbulent regime. Both the momentum and energy equations are solved during this phase to capture the convective heat transfer. After reaching steady-state flow conditions, the momentum equation is switched off, and a constant velocity profile is applied. Subsequent simulations focused solely on solving the energy equation in this zone.

The eutectic alloy region is modeled using laminar flow and energy equations, heat conduction, melting/solidification, and natural convection effects. To implement this convection effect, the buoyancy force that drives the density difference must be solved numerically using Boussinesq approximation, as illustrated in [equation \(12\)](#). This approximation treats the temperature dependency of the density and allows the distribution of natural heat convection [32].

$$f_b = \rho g \beta (T_{ref} - T) \quad (12)$$

Where f_b is the body force term, g is the gravity acceleration [m/s^2], T_{ref} is the reference temperature [K], and T is fluid temperature [K].

4. Results

4.1. Model Validation

The validation of the numerical model is conducted by comparing simulated and experimental temperature responses. Figure 4.1 displays temperature profiles at six radial positions (4A to 4F) during both charging and discharging phases, providing insight into the model's accuracy in capturing phase change dynamics.

The simulation successfully captures the general trend of the phase change process, with melting and solidification periods aligning well with experimental observations. However, certain mismatches can be seen, particularly in the solidification phase. During melting, simulations exhibit a relatively stable temperature plateau at the eutectic point, whereas experimental data show a gradual increase and fluctuation, likely due to residual heat absorption and external factors in the real physical model. These suggest that thermal inertia effects in the physical system are not fully captured in the model. In the discharging phase, simulations predict a uniform solidification radially outward, while the experimental data reveal delayed cooling at central positions (4C to 4E). It is possibly because of the bidirectional heat extraction through HTF-contacted end caps, as stated in the reference data of the experiment. The bidirectional energy transfer is absent from the model due to the exclusion of detailed flange geometry for simplification purposes. Furthermore, the solidification time of the model is a little longer than the validation due to this feature, as the energy is extracted from just the PCM contact boundary. These mismatches highlight the model's limitations in representing complex boundary interactions and underscore the need for improved geometric and heat transfer modeling. Nonetheless, the model demonstrates reliable prediction of overall thermal behavior and phase change duration, with melting and solidification times within approximately 5% of the experimental values.

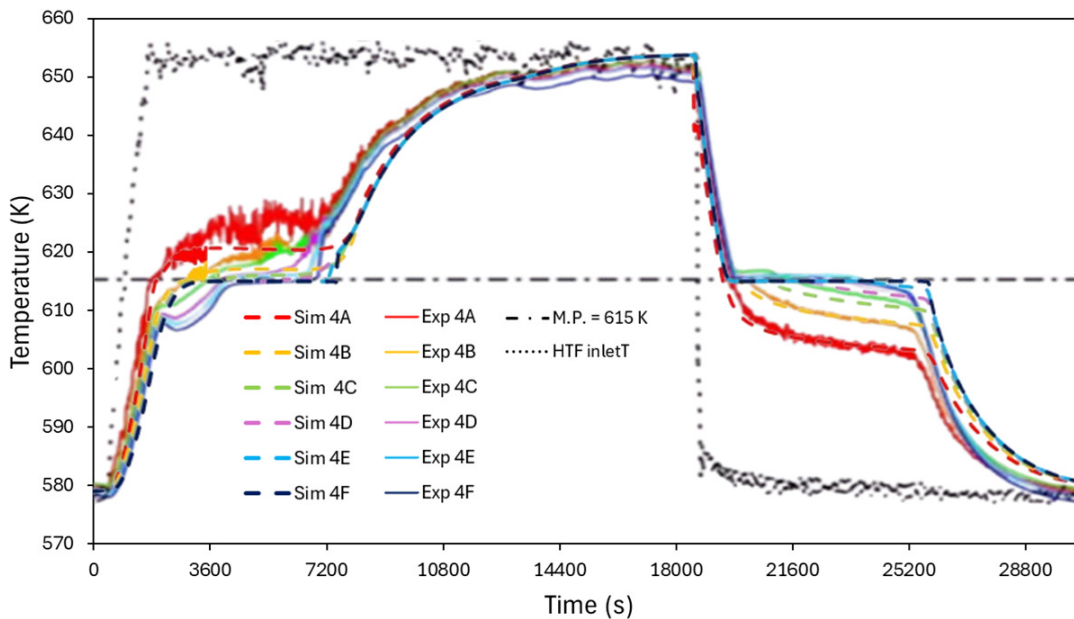


Figure 4.1. Comparison between the simulation result and experimental data, observing the thermocouples A to F on sheath four during the charging and discharging process.

4.2. Simulation Result

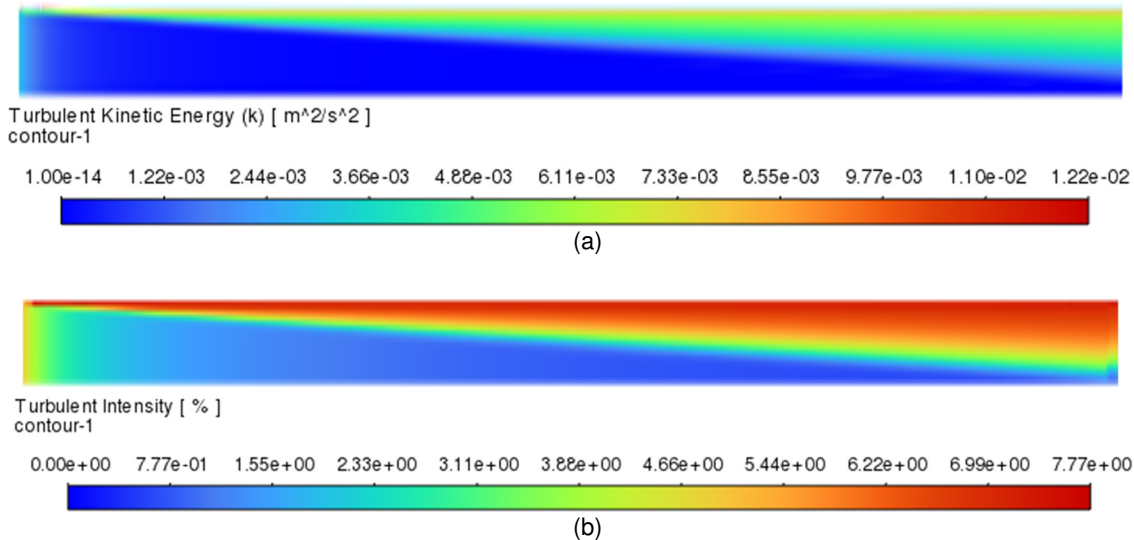
4.2.1. Flow Profile of Oil Domain

According to the model description, the Reynolds number can be calculated from [equation \(13\)](#), which yields approximately 68,800. It's aligned with the selected k- ω SST model, as the number indicates fully turbulent flow in the oil domain.

$$Re = \frac{\rho v D}{\mu} \quad (13)$$

The simulation results show a shear-driven turbulence structure within the oil domain. The contour of turbulent kinetic energy (k_t) reveals that turbulence is concentrated along the pipe wall's boundary layer, indicating that wall shear generates turbulence. However, the central region of the oil flow remains nearly laminar, with minimal turbulent activity. Supporting this, the distribution of turbulent intensity further confirms the localized turbulence generation. The high intensity is observed near the inlet and along the boundary at up to 7.77%, where strong shear and velocity fluctuations dominate. Both values, as shown in [Figure 4.2a](#) and [4.2b](#), confirm the presence of wall-bounded turbulence, enhancing local mixing and convective heat transfer.

Additionally, during the solidification process, a similar shear-induced turbulence structure is observed, even though the HTF flow is in the opposite direction. This behavior is displayed in [Figures 4.2c](#) and [4.2d](#), where turbulent kinetic energy and intensity contours reveal boundary-layer turbulence near the pipe wall as well. Lastly, although the non-dimensional distance y^+ value between 14 and 25 in [Figure 4.3](#) are not ideal, they fall within an acceptable range for this SST model. Further mesh refinement could improve near-wall accuracy, but the computational cost of this simulation is limited.



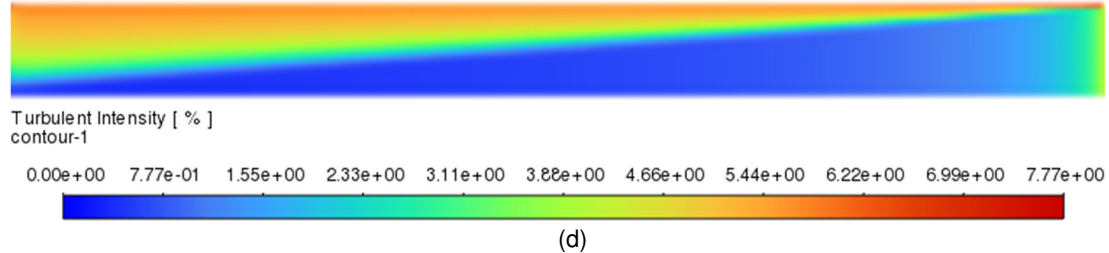
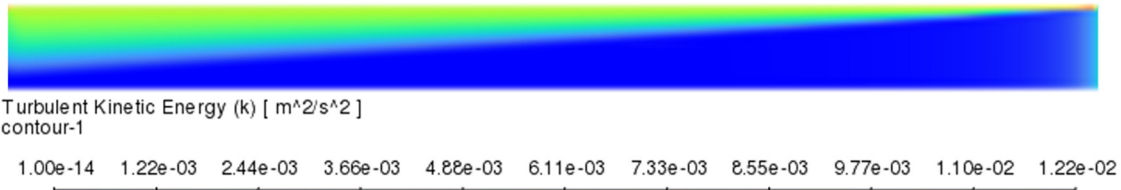


Figure 4.2. a) Turbulent kinetic energy [m^2/s^2] and b) Turbulent intensity [%] contour of the oil domain at a steady state during the melting process. c) Turbulent kinetic energy [m^2/s^2] and d) Turbulent intensity [%] contour of the oil domain at steady state during the solidification process.

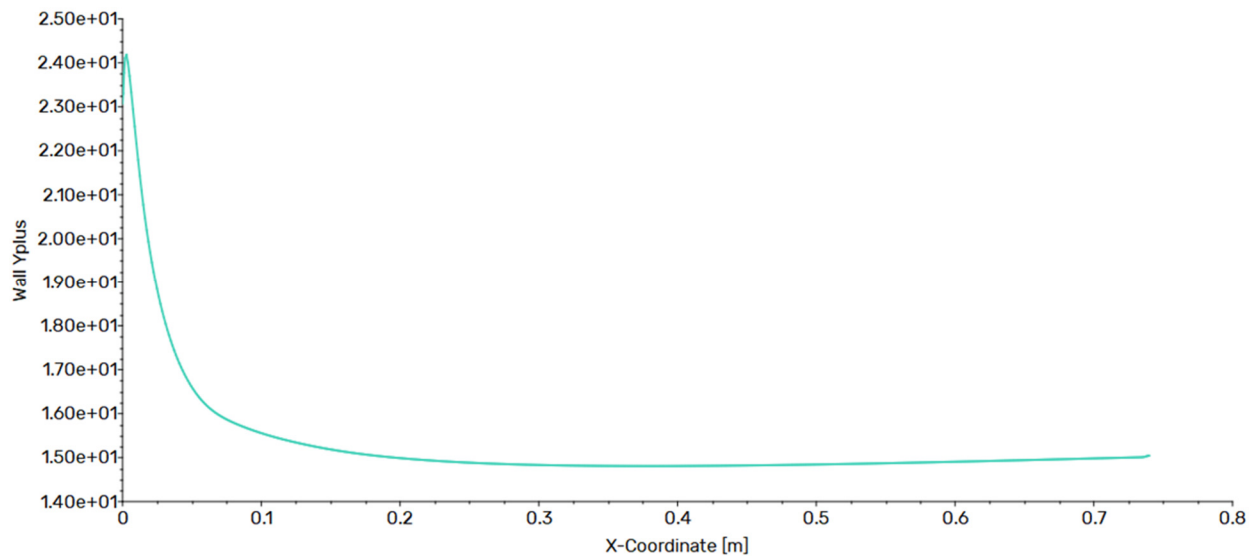


Figure 4.3. Wall y^+ value along the oil domain inner wall

4.2.2. Temperature Profile

The temperature profile provides a detailed understanding of heat distribution and thermal behavior within the TES during the charging and discharging cycles. Figures 4.4 and 4.5 present the evolution of temperature, highlighting key thermal gradients and identifying the influence of natural convection during the phase change process in axial and radial directions, respectively.

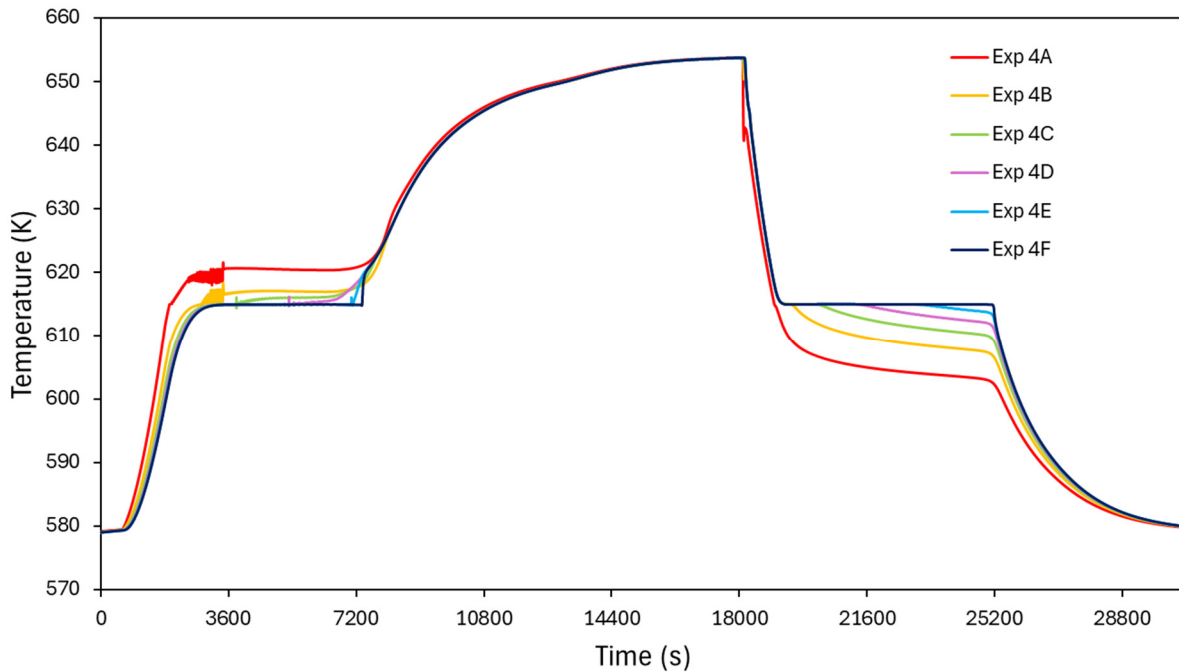
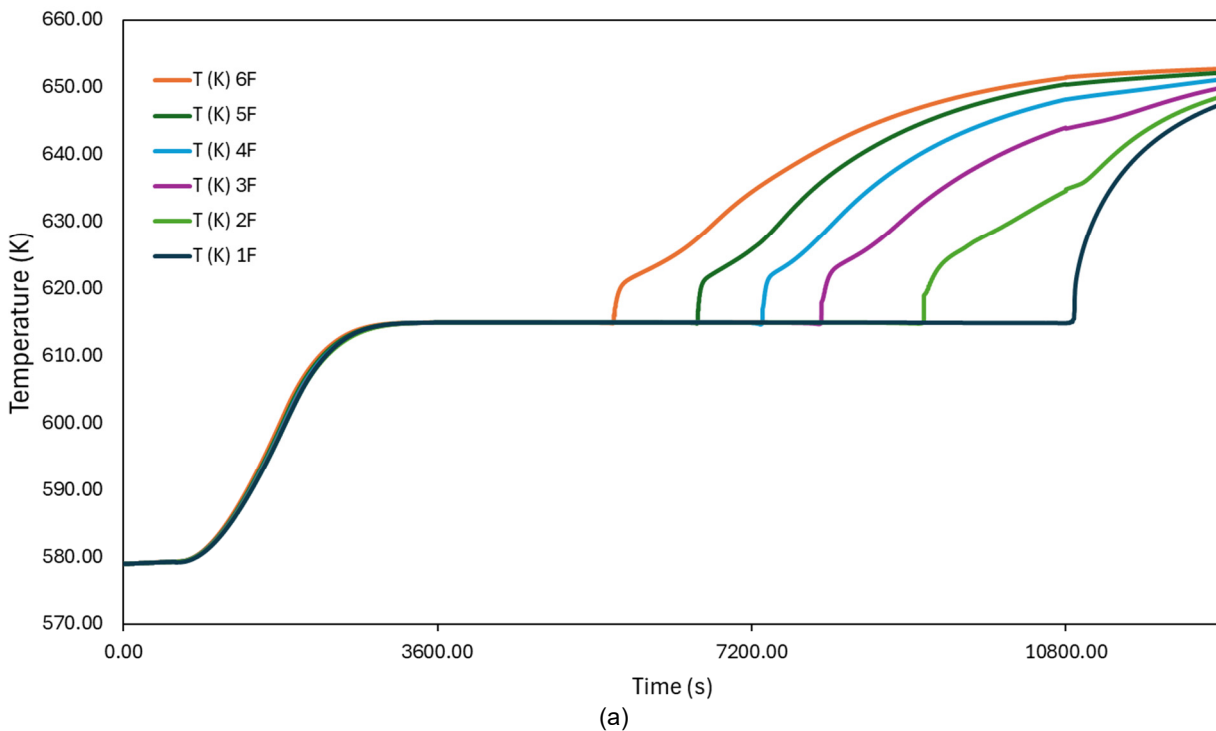


Figure 4.4. Temperature evolution of thermocouples A to F on sheath four



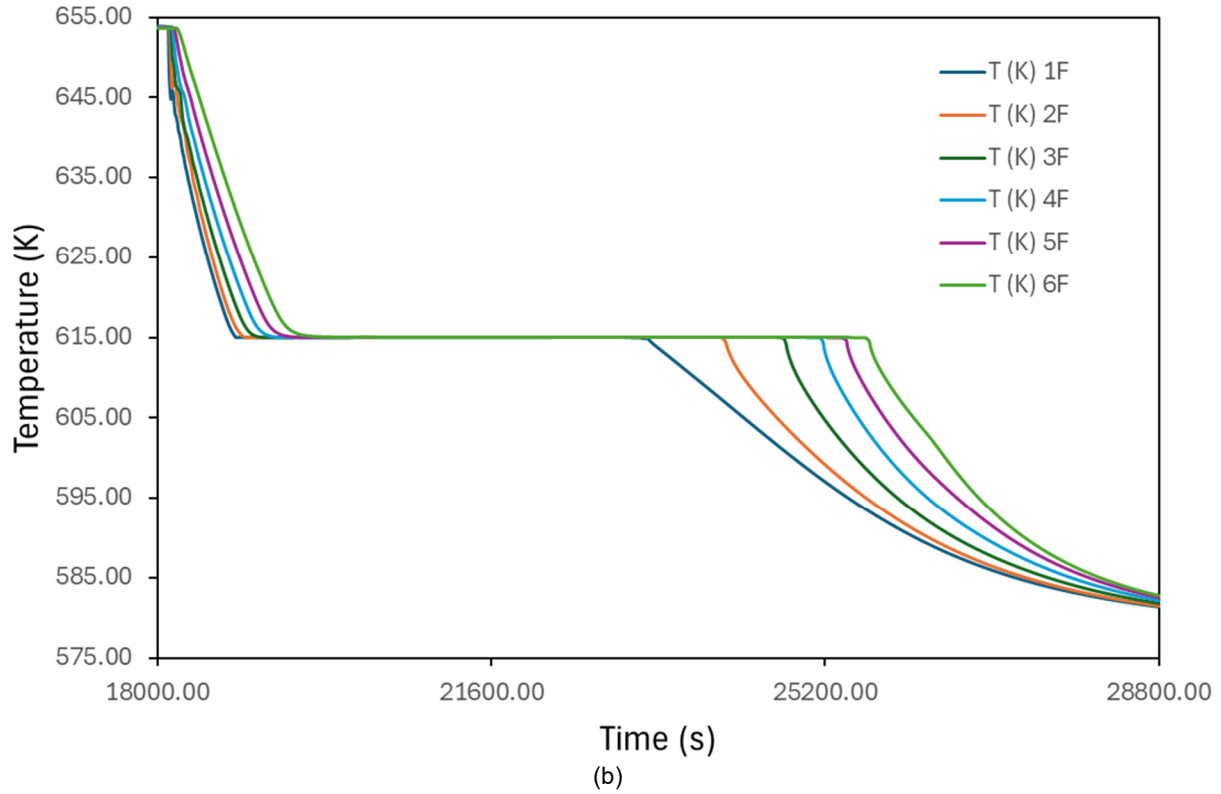


Figure 4.5. Temperature evolution of thermocouple F of all sheathes during a) melting, and b) solidification.

Figure 4.4 presents the radial temperature evolution observed by thermocouples 4A to 4F during the charging and discharging cycles, highlighting the transient behavior of the eutectic Mg₄₉Zn₅₁ alloy. Melting starts when the innermost sensor 4A reaches the eutectic temperature of approximately 615 K and finishes once the outermost sensor 4F. Before the melting, a steep temperature rise is shown due to sensible heat, followed by a distinct plateau between approximately 2000 and 7400 seconds, indicating isothermal conditions during the phase transition and confirming uniform heat transfer across this region. After complete melting, the temperature continues to rise gradually to the HTF temperature as heat transfer shifts to a combination of conduction and natural convection within the molten alloy, which has lower thermal conductivity. Upon discharging, a sharp temperature drop at around 18,300 seconds marks the onset of heat release. The solidification occurs between approximately 19,200 and 25,200 seconds, exhibiting a plateau at the eutectic point. The cycle ends with a progressive decrease in temperature toward the oil inlet condition at about 579 K, indicating the completion of solidification for all monitored positions.

The temperature evolution recorded by external thermocouples, particularly position F, in sheaths 1 to 6, reveals the spatial progression of melting and solidification within the system displayed by Figure 4.5. During the melting process, the temperature profiles clearly indicate that the phase front transitions from top to bottom, consistent with heat supplies from the top and internal regions. Conversely, solidification occurs from bottom to top due to the inverse oil flow direction. These results show the heat dissipation according to the expected dynamics of the heat source.

4.2.3. Melting and Solidification Time

The efficiency of latent heat storage systems is strongly influenced by the time required for complete melting and solidification of the PCM. [Table 4.1](#) shows the time dependence of the outermost interfaces, specifically thermocouples F, along the axial direction of both processes. The model's ability to capture transient phase change dynamics and the effect of natural convection is evaluated by comparing the times under these specific thermal conditions.

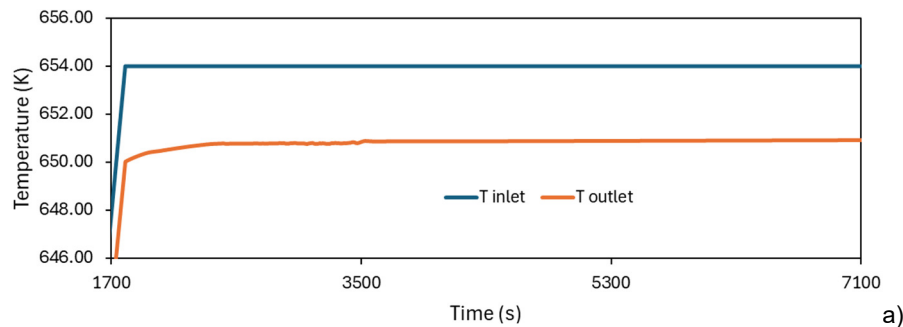
Table 4.1 Melting and solidification times as a function of sheath position.

| Sheaths | 1 | 2 | 3 | 4 | 5 | 6 |
|-------------------------|------|------|------|------|------|------|
| Melting time (s) | 8475 | 7180 | 5800 | 4970 | 4180 | 3220 |
| Solidification time (s) | 4600 | 5200 | 5800 | 6000 | 6100 | 6100 |

The number reveals that the estimated total time required to melt the PCM within the system is 140 minutes, and complete solidification is achieved by around 100 minutes, indicating that solidification occurs approximately 30% faster than melting. The observed durations arise primarily from the internal heat transfer dynamics between oil and eutectic alloy, defined in the numerical model.

One of the factors that can affect the melting and solidification time is the temperature difference between the inlet and outlet temperatures, as they drive the heat transfer along the boundary. The inlet and outlet temperature profiles during the melting in [Figure 4.6a](#) and solidification in [Figure 4.6b](#) provide additional insights into the thermal behavior of the TES system. During the melting process, the inlet temperature is kept constant at 654 K, resulting in the outlet temperature gradually rising and stabilizing slightly below the inlet. It indicates effective heat absorption by the PCM and consistent convective transfer through the system. In contrast, during solidification, outlet temperatures show a more decline to the constant inlet temperature of 579 K. This suggests reduced thermal gradients and a more conduction-driven process. These differences imply that heat exchange during charging is more efficient rate. However, as the total solidification time is less than the melting time, it indicates that the change in thermophysical properties is more significant compared to the temperature difference. This phenomenon will be discussed further in the next section.

Lastly, the simulation set for that time is purely dependent on the inner surface because the other interfaces are defined to be insulated. Nevertheless, the solidification time does not entirely match the validation data due to the real physical geometry, as discussed in the model validation section.



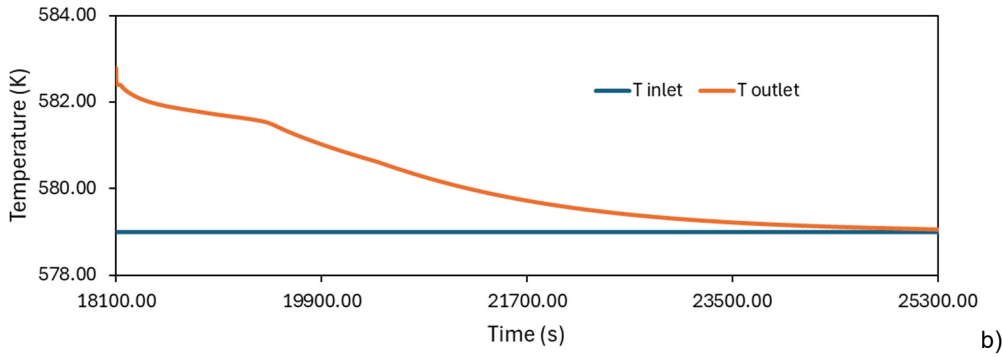
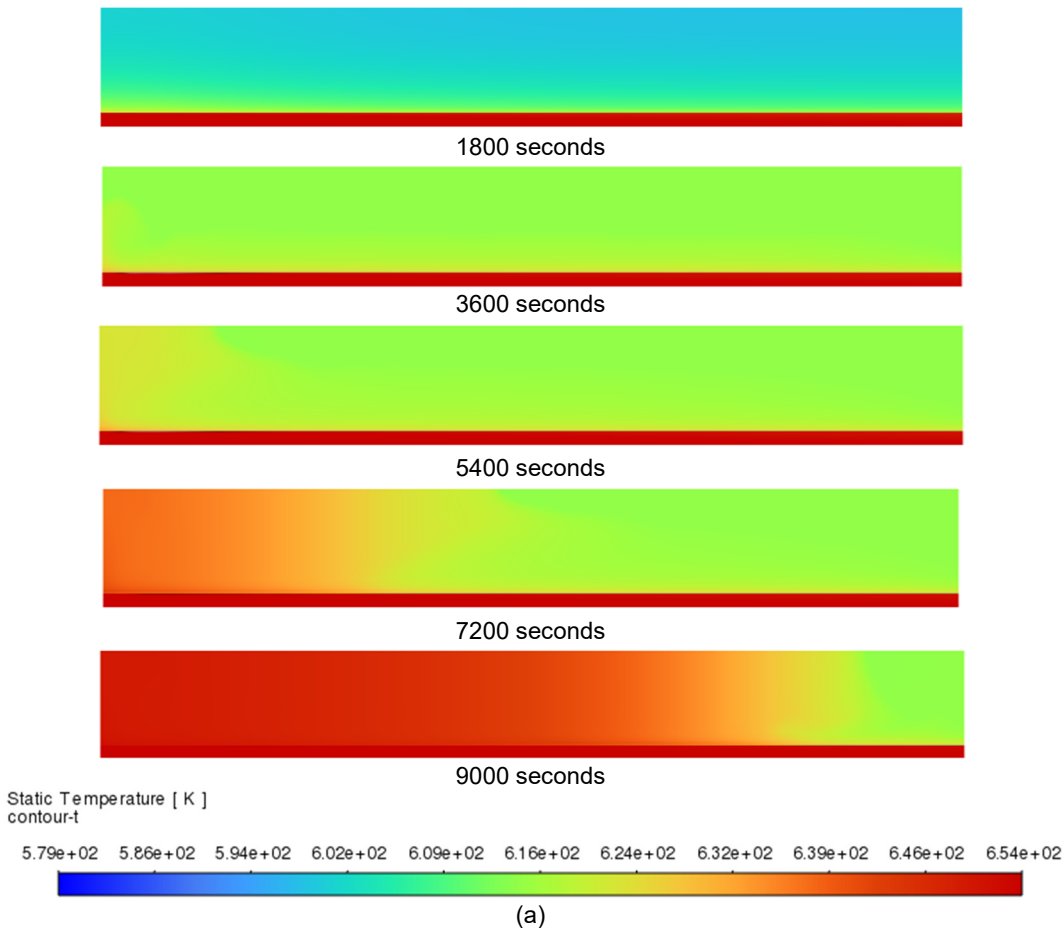
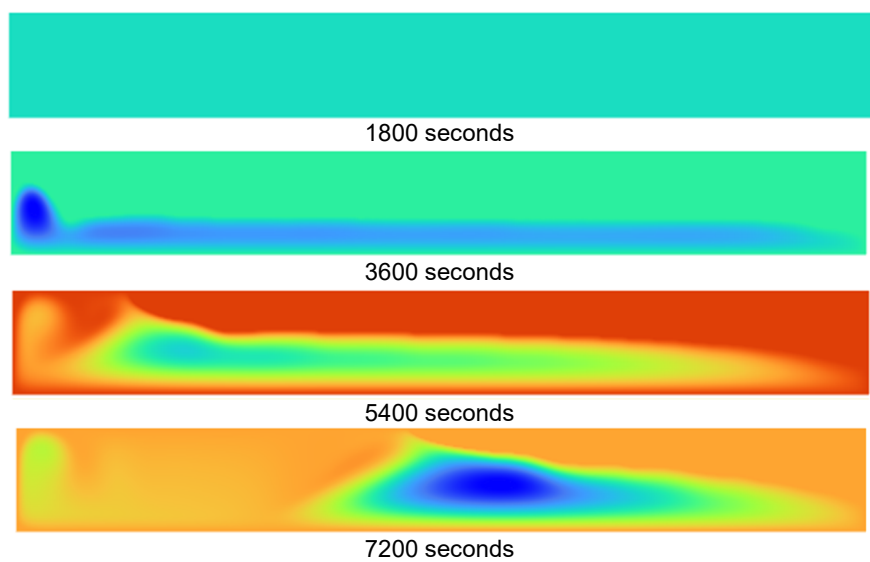
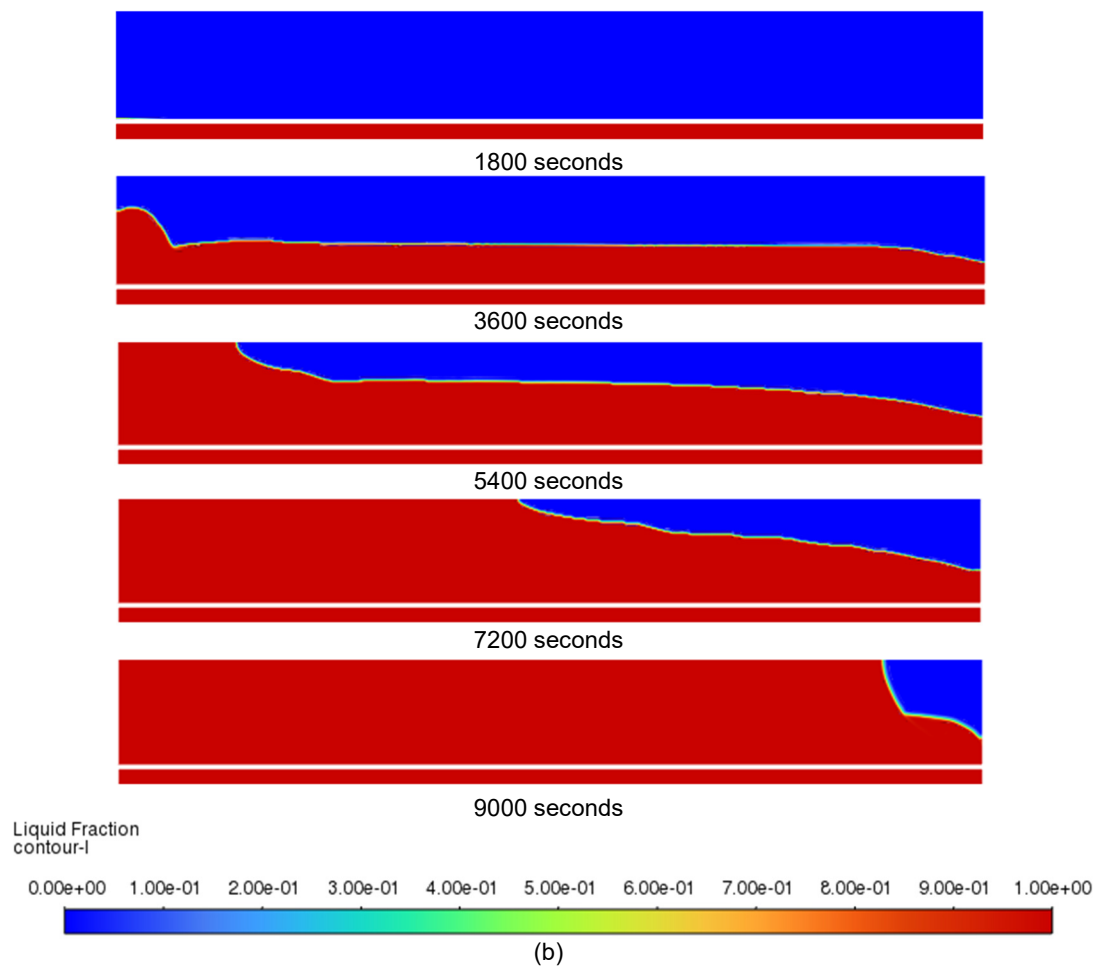


Figure 4.6. Temperature differences between the inlet and outlet during a) melting, and b) solidification.

4.2.4. Graphical Visualization of Melting Process

Graphical visualization is crucial in interpreting complex simulation results, especially when dealing with multiphase and transient simulations. This section includes contours of different thermophysical properties in the alloy region, representing the thermal and fluid flow behavior. [Figure 4.7](#) presents contour plots of liquid fraction, temperature, and stream function during the charge phase. The figures show the visualization of a particular time to observe the evolution of different parameters for these processes and offer a progressive illustration of the eutectic.





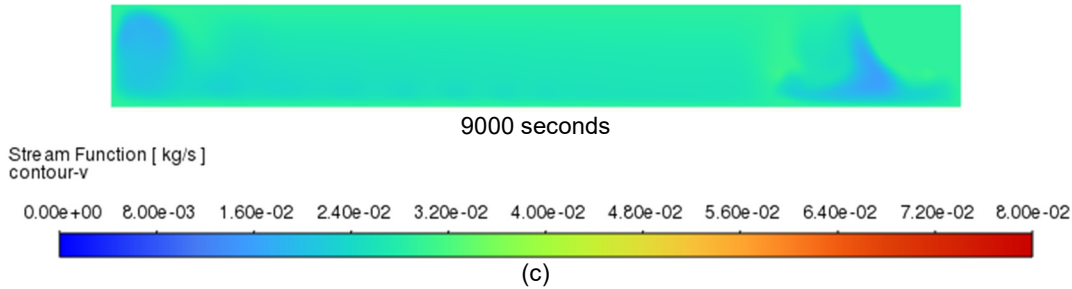
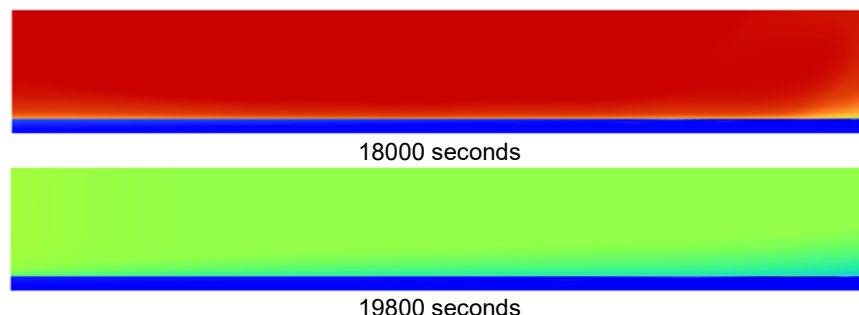


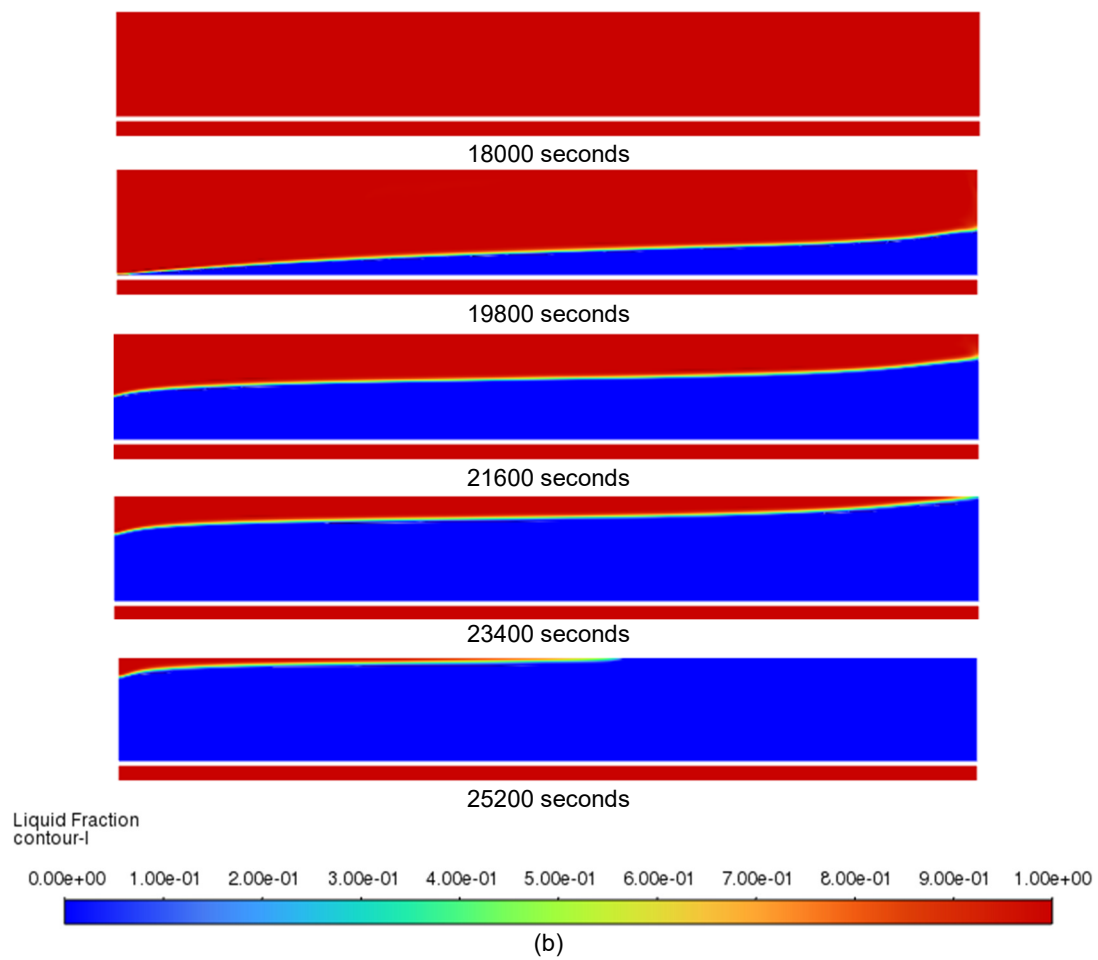
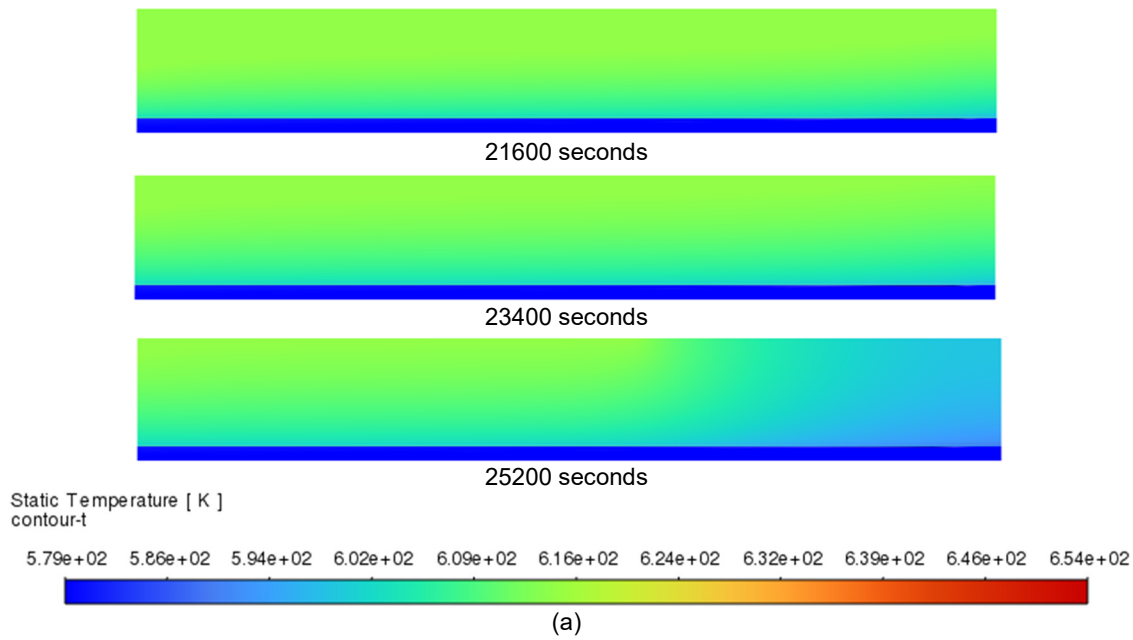
Figure 4.7. Contour of a) temperature (K), b) liquid fraction, and c) stream function (kg/s) in 1800, 3600, 5400, 7200, 9000 seconds during the melting process.

During the melting process, as shown in [Figure 4.7](#), conduction-dominated conditions are expected initially as the majority of the PCM is still in a solid state. The temperature contours at early stages show a smooth, radially outward temperature gradient from the heat source, confirming that heat transfer is governed by conduction. After 3,600 seconds, the temperature profile begins to rise more noticeably from the top region of the TES, indicating the development of heat convection in the downward direction. At this specific time, the liquid fraction contours reveal that the melting front does not progress uniformly, especially in the lower domain, which supports the presence of buoyancy-induced circulation and natural convection. The stream function contours also support this observation, showing a weak circulation forming near the heated boundary at 3,600 seconds, which aligns with the early phase of melting and the onset of buoyancy-driven flow. As the melting continues and more of the PCM transforms into liquid at 5,400 and 7,200 seconds, the stream function contours show stronger and better-defined convection patterns. The higher stream function magnitudes indicate more intense fluid motion, and enhanced convective flow significantly boosts heat transfer efficiency in the liquid region. However, by 9,000 seconds, a gradual weakening of fluid circulation can be seen because the temperature becomes more uniform. Despite this, convective patterns during the earlier stages also play a crucial role in accelerating the melting process and ensuring the redistribution of thermal energy throughout the PCM. The contour describes a dynamic transition from conduction to convection-dominated heat transfer and natural convection in the simulation.

4.2.5. Graphical Visualization of Solidification Process

The visualization of the contour of the temperature, liquid fraction, and steam function during the discharge phase is presented in this section. The features like inverse oil flow and natural convection, as mentioned in [section 4.2.3](#), can be better demonstrated using the progressive evolution of different parameters in this graphical form, as shown in [Figure 4.8](#).





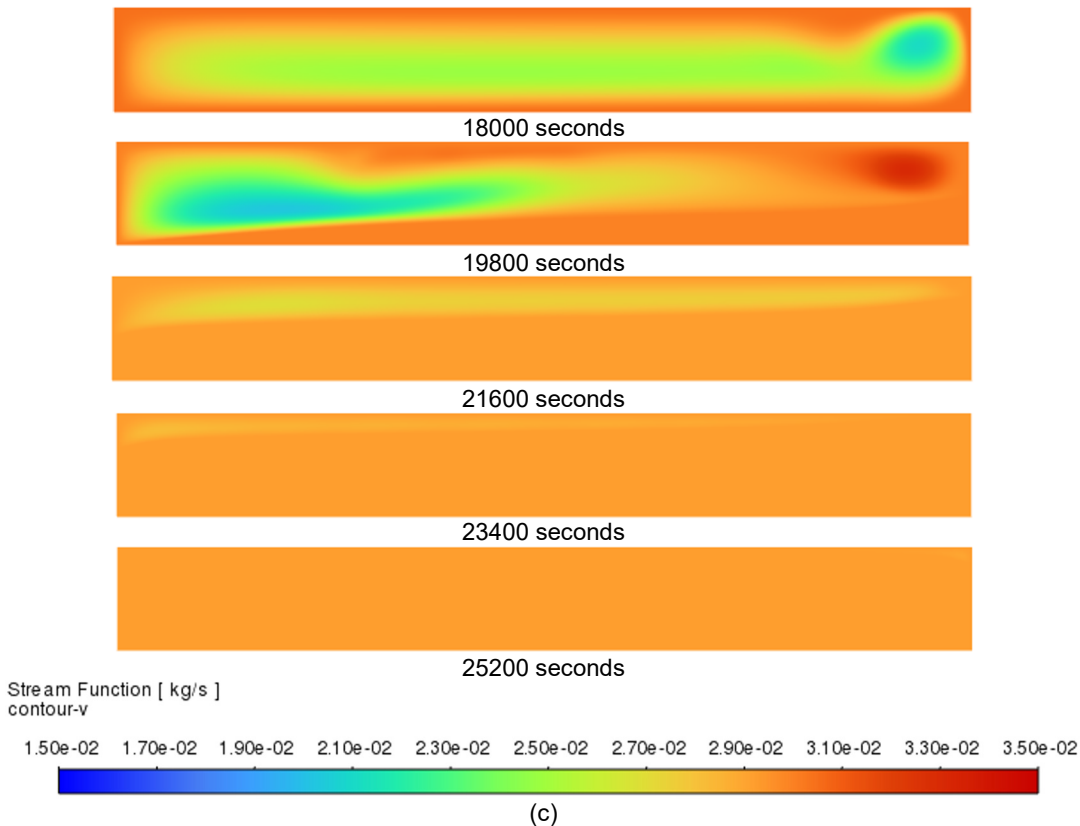


Figure 4.8. Contour of a) temperature (K), b) liquid fraction, and c) stream function (kg/s) at 18000, 19800, 21600, 23400, 25200 seconds during the solidification process.

The figure reveals thermal fluid interactions during the discharging process. Initially, cold oil is introduced at the inlet at the bottom of TES, while the temperature is still high at 654 K. Therefore, heat extraction is observed from the upward oil flows. From the beginning of discharge to the next 1,800 seconds, there is an abrupt change in temperature, and an even distribution of temperature profile is shown. Moreover, a thermal gradient gradually develops from bottom to top, consistent with the reversed HTF direction. Liquid fraction contours confirm this as PCM solidifies from the outlet side upward and show a more uniform pattern compared to the charging process. The stream function contours highlight reduced convective strength compared to melting, especially at later times from 21,600 to 25,200 seconds, as the temperature drops dramatically. This weaker circulation zone and diminished fluid motion suggest that convection has a less significant role during solidification. The reduced buoyancy forces in the cooler domain during solidification lead to a more uniform heat dissipation dominated by conduction, resulting in a more linear and symmetric front propagation. To conclude, the contour for solidification can well validate the transient asymmetry and the impact of directional flow effects in the eutectic region.

5. Implications of the Simulation Model

5.1. Impact of HTF Flow Direction

As the HTF flows direction of the validation data is upward, the impact of different flow directions on the solidification of PCM is worth observing further. Figure 5.1 compares the temperature evolution during the discharging process at two axial thermocouple positions, 1F and 6F, under two different HTF flow directions. In both cases, the solidification starts rapidly and then transitions into a slower temperature decrease as the PCM releases latent heat. Notably, when the HTF flows downward, the temperature at both 1F and 6F remains at the eutectic temperature for a longer duration compared to the upward flow case. This indicates that solidification is delayed under downward flow conditions. This phenomenon is likely due to thermal buoyancy effects. With downward HTF flow, the cooler oil enters from the top, which opposes the natural convection within the molten PCM that typically circulates warm liquid upward. This excess convective heat transfer leads to less effective cooling and prolongs solidification, unlike upward HTF flow. Moreover, according to the chart, the estimated total time of solidification is 6,100 and 7,200 seconds for upward and downward direction, respectively. It shows that the upward flow of HTF solidifies the PCM around 18% faster than the opposite direction.

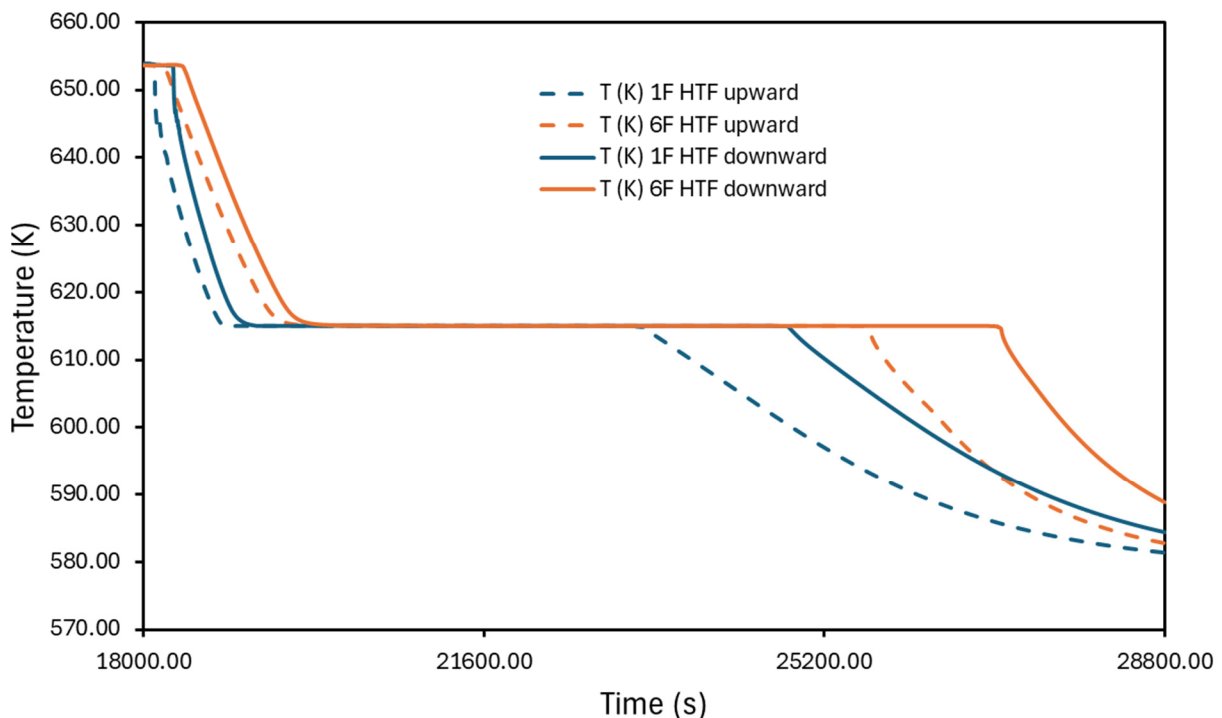


Figure 5.1. The temperature evolution during PCM solidification at thermocouple 1F and 6F, under upward (dashed line) and downward (solid line) HTF flow directions.

In addition, Figure 5.2 illustrates the evolution of liquid fraction contours in the PCM domain for these different HTF flow directions. These contour plots provide a clear impact of the direction of the progression of the solidification front. The model describes upward flow as from right to left and vice versa for downward flow. For the upward case, the solidification initiates more rapidly from the bottom and progresses to the top with a steeper solidification gradient.

Conversely, for the downward-flow case, the cooling front progresses more gradually and uniformly from top to bottom, indicating slower heat extraction near the outlet region at the bottom. At each time step, the downward flow consistently retains a larger liquid fraction, confirming that the upward flow accelerates solidification. This effect is primarily due to natural convection, where cooler HTF entering from below maximizes the driving temperature gradient for heat extraction. These results demonstrate that heat source flow direction can significantly influence the thermal behavior of the system during discharge, and optimizing flow configuration could be a key strategy to improve system efficiency.

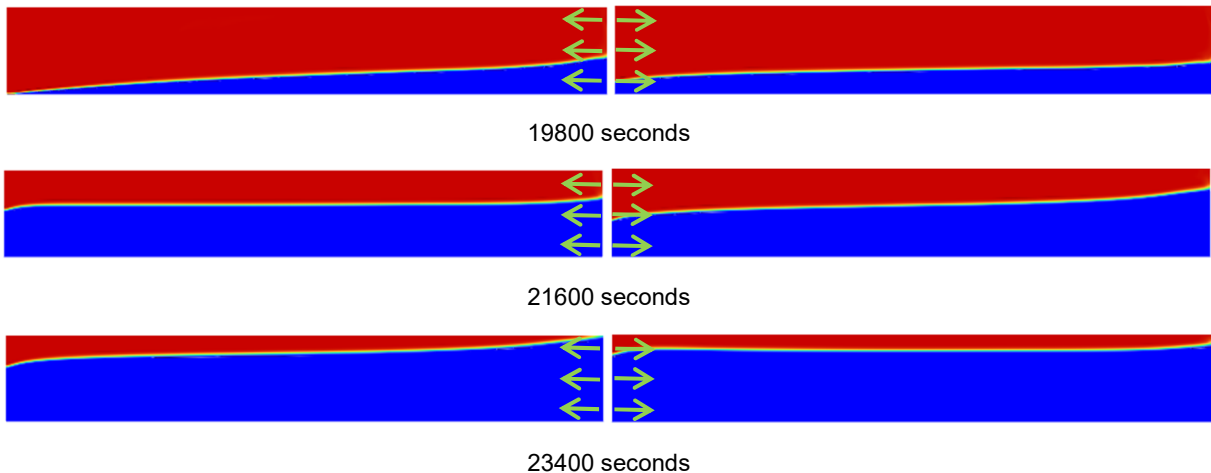


Figure 5.2. Liquid fraction contour of PCM during the solidification process, HTF upward (left) and downward (right) flow direction, represented by green arrow, at times 19,800, 21,600, and 23,400 seconds.

5.2. Impact of HTF Flow Inlet Velocity

Velocity is one of the critical parameters that affect the heat transfer mechanism of TES because it can alter the flow dynamics. According to [equation 13](#), the parametric change of velocity has a direct relation to Reynolds' number and can weaken or strengthen the turbulence, which is discussed in this section.

[Figure 5.3](#) presents the contours of turbulent intensity within the oil domain for three different HTF inlet velocities at 0.5 m/s, 1 m/s, and 2 m/s. At the lowest velocity, the intensity is very low at less than 5%, indicating a near-laminar regime. At 1 m/s, which is the baseline case, moderate turbulent intensity develops along the boundary layer, showing improved turbulence and enhanced local mixing. At 2 m/s, the turbulent intensity is significantly higher, around 20%, especially near the inlet and the wall. This strong convective motion contributes to better heat transfer between the two domains. Furthermore, [Figure 5.4](#) illustrates the turbulent kinetic energy contours for the same three inlet velocities. The values are very low and close to zero for the whole region at 0.5 m/s of HTF flow. At 1 m/s, the kinematic energy slightly increases and becomes more crucial along the pipe walls, corresponding to the wall-generated turbulence. When the inlet velocity is set to 2 m/s, the value reaches much higher and extends into the core of the flow near the outlet. This higher turbulent kinetic energy results in more effective thermal energy transfer to PCM because of the high energy content near the wall.

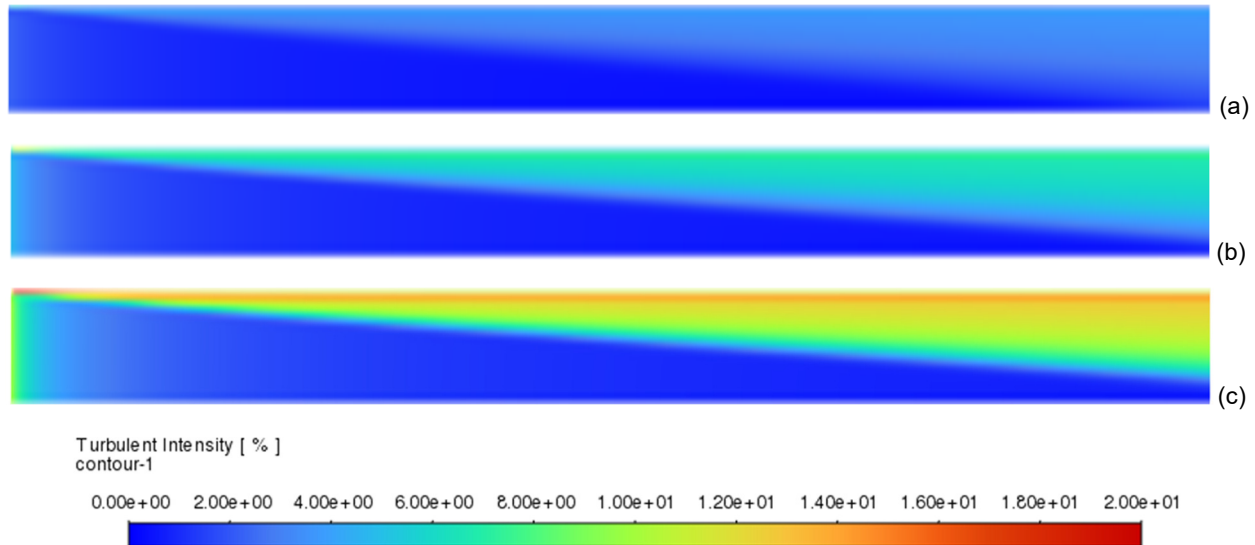


Figure 5.3. Turbulent intensity [%] contour of the HTF domain at HTF inlet velocity of a) 0.5 m/s, b) 1 m/s, and c) 2 m/s

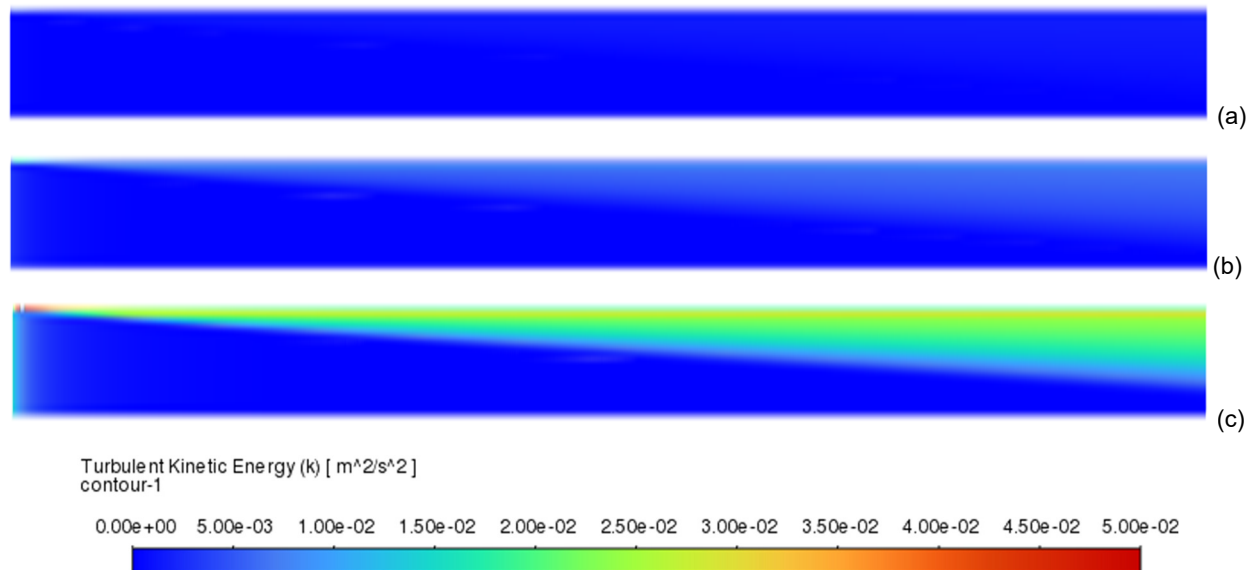


Figure 5.4. Turbulent kinetic energy [m^2/s^2] contour of the HTF domain at HTF inlet velocity of a) 0.5 m/s, b) 1 m/s, and c) 2 m/s

Additionally, [Figure 5.5](#) shows the evolution of the integral of liquid fraction over different velocities during the melting process. The results clearly demonstrate that increasing the HTF inlet velocity significantly accelerates the melting rate of PCM. At 9,000 second, the liquid fraction reaching about 32 m^2 , 39 m^2 , and completely melt at 42.21 m^2 , for the velocity of 0.5 m/s, 1 m/s, and 2 m/s, respectively. This enhanced melting performance directly corresponds to the reason that higher velocities resulted in greater turbulent kinetic energy, particularly near the heated boundary. The turbulent flow increases the temperature gradient at the PCM boundary, thereby promoting faster and more uniform melting.

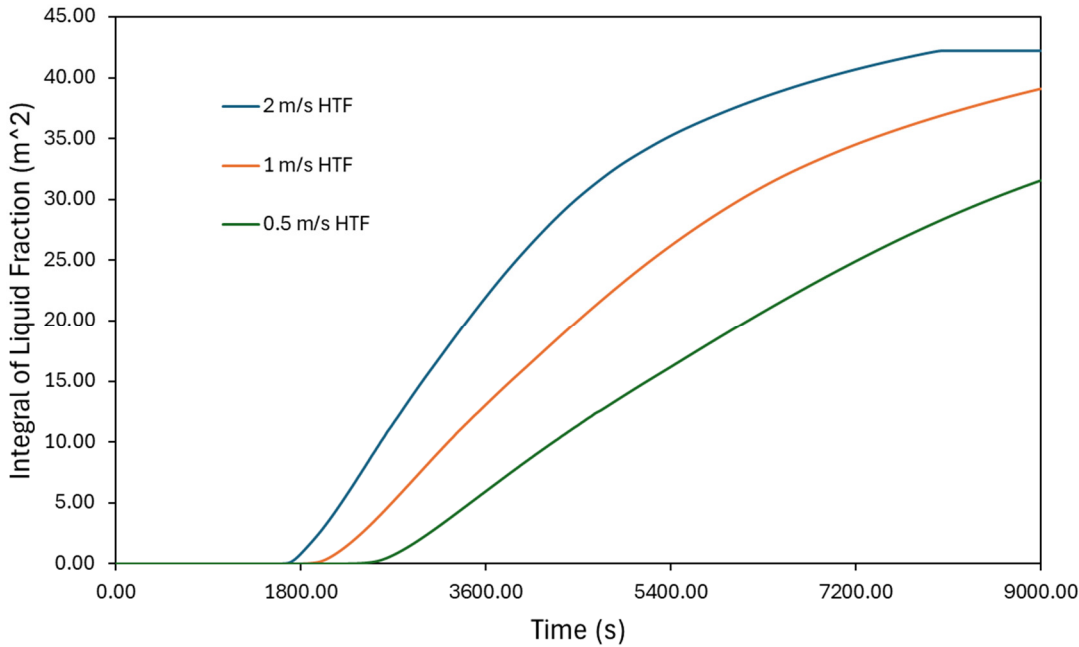


Figure 5.5. Integral of liquid fraction [m^2] chart of the HTF domain at HTF inlet velocities of 0.5 m/s, 1 m/s, and 2 m/s.

To further evaluate the thermal performance of the latent heat storage system, the temporal evolution of enthalpy absorbed and stored in the PCM, as shown in Figures 5.6 and 5.7, respectively, is investigated.

The enthalpy absorbed can be determined by integrating the enthalpy difference between the inlet and outlet over time, while the enthalpy stored is calculated by the integral of the enthalpy of the whole PCM domain as a function of time. Both figures show consistent increases in absorbed and stored enthalpy with rising HTF inlet velocity. In Figure 5.6, the absorbed enthalpy increases steadily over time for all cases, with the 2 m/s flow achieving the highest absorbed energy at around 15,000 kJ, followed by 1 m/s and 0.5 m/s at approximately 12,000 kJ and 10,000 kJ, respectively. This indicates that higher HTF velocity provides more rapid and sustained energy transfer into the PCM domain. In Figure 5.7, the stored enthalpy in PCM also increases with the same trend with the initial enthalpy at 13,986 kJ from the internal energy of PCM at initial temperature. The stored enthalpies of around 24,900 kJ, 23,900 kJ, and 21,500 kJ are reached by HTF velocity at 2 m/s, 1m/s, and 0.5 m/s, respectively. This aligns well with the expected physical behavior during the melting process, where the enthalpy rises accordingly. These results provide a basis for evaluating thermal performance and support accurate thermal efficiency calculations based on the stored-to-absorbed enthalpy ratio.

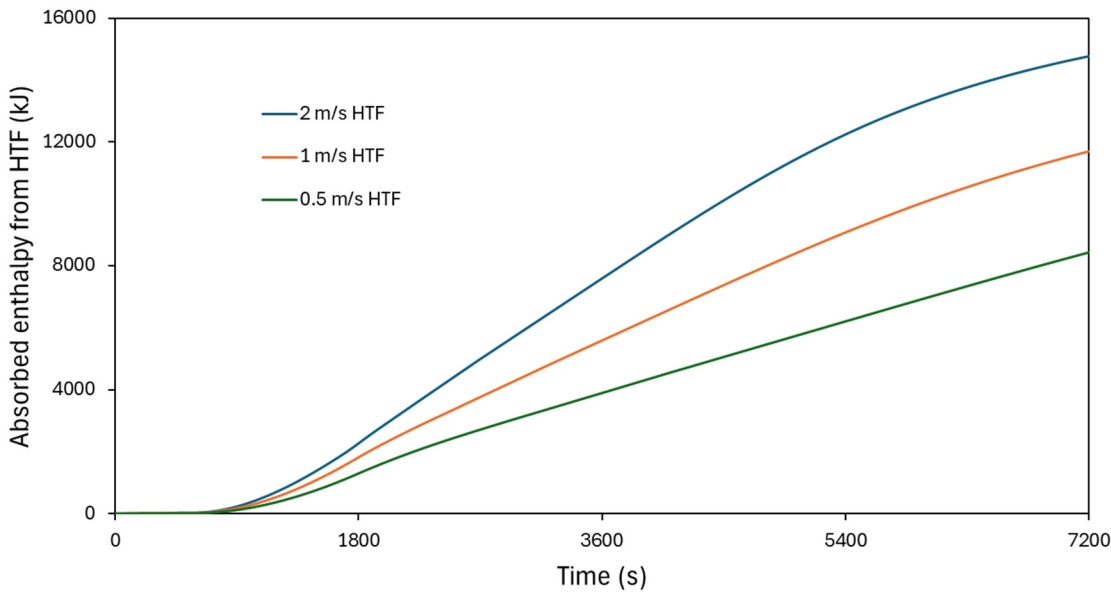


Figure 5.6. Absorbed enthalpy [kJ] from HTF to PCM at HTF inlet velocities of 0.5 m/s, 1 m/s, and 2 m/s.

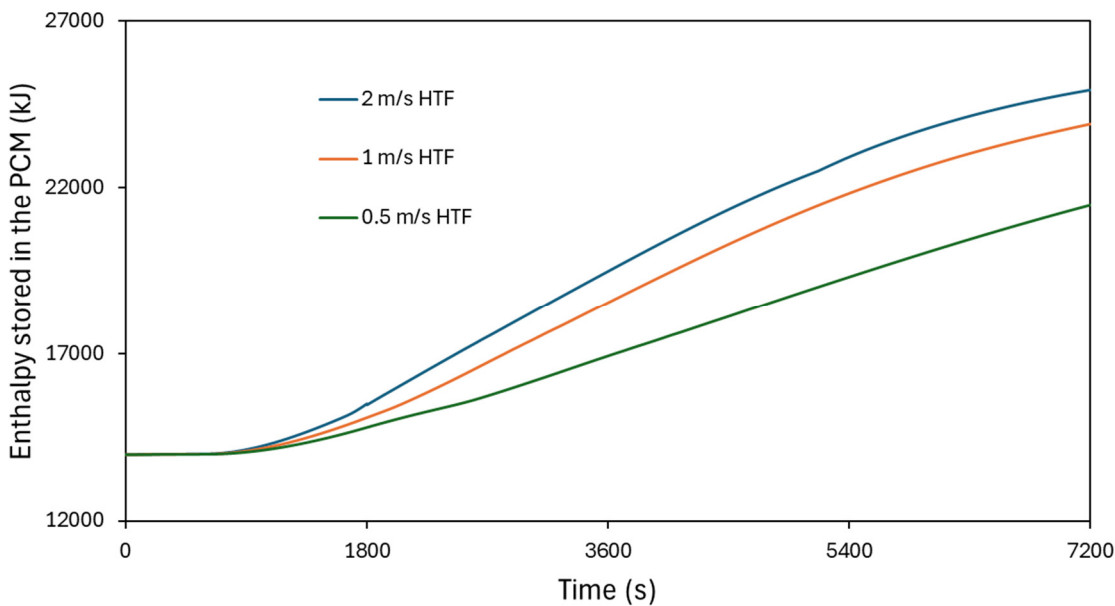


Figure 5.7. Enthalpy stored in the PCM [kJ] as a function of time in PCM at HTF inlet velocities of 0.5 m/s, 1 m/s, and 2 m/s.

The thermal efficiency (η) is calculated as defined in [Equation \(14\)](#) as the ratio of the stored enthalpy in the PCM to the total absorbed enthalpy from the HTF over time. The equation reflects the physical interpretation of how efficiently the system converts absorbed thermal energy into stored energy within the TES domain.

$$\eta = \frac{h_{stored}}{\int_{t_0}^{t_f} (\dot{h}_{out} - \dot{h}_{in}) dt} \quad (14)$$

where \dot{h}_{out} [J/s] and \dot{h}_{in} [J/s] are the outlet and inlet enthalpies, and h_{stored} is the enthalpy stored in PCM.

As mentioned, the stored enthalpy comprises internal energy at a given temperature, together with accumulated energy from sensible and latent heat through the process. It is calculated as the integral of the enthalpy of the PCM domain.

[Figure 5.8](#) and [Table 5.1](#) show the temporal evolution of this efficiency across three HTF inlet velocities and overall thermal efficiency, respectively. Although the 2 m/s case demonstrates faster heat absorption, the initial efficiency reaches approximately 70% and remains at this level with minimal fluctuation over time. The rapid flow limits energy transfer duration despite a higher total heat input and leads to the lowest overall thermal efficiency at 74.12%. In contrast, 0.5 m/s flow achieves the highest efficiency at around 88.93%, benefiting from extended transfer duration and better energy retention despite absorbing less total heat. The 1 m/s case balances both overall efficiency and energy transfer duration. These results underscore the importance of optimizing flow rates not just for energy delivery but also for maximizing storage efficiency in real-world TES applications. However, the efficiency trend and its inconsistency still provide a gap for further study, as well as overall TES system efficiency, which will be mentioned in the next section.

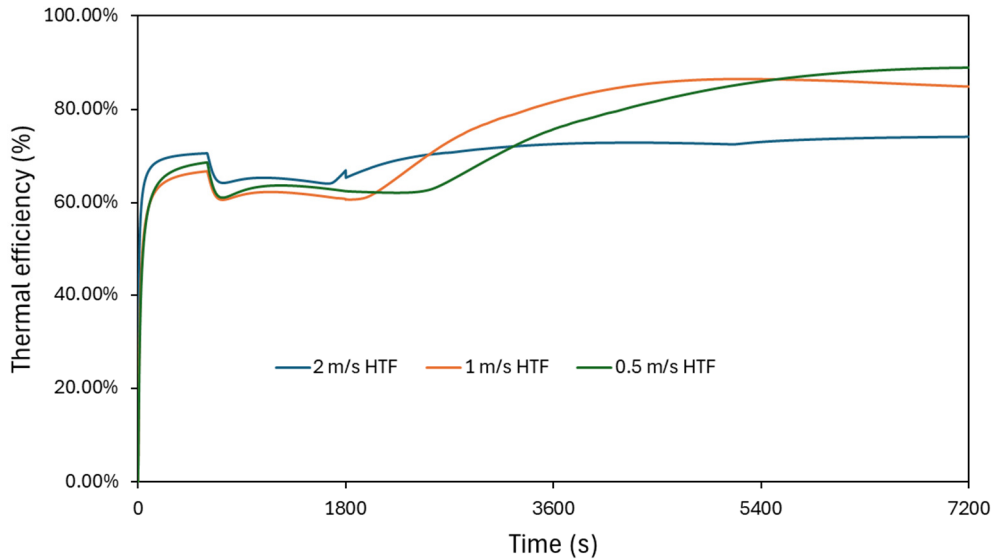


Figure 5.8. Thermal efficiency [%] from charging start to 7,200 seconds at oil inlet velocities of 0.5 m/s, 1 m/s, and 2 m/s.

Table 5.1 Total absorbed and stored enthalpy and overall thermal efficiency from charging start to 7,200 seconds at HTF inlet velocities of 0.5 m/s, 1 m/s, and 2 m/s.

| HTF velocity inlet | 2 m/s | 1 m/s | 0.5 m/s |
|--------------------------------|--------|--------|---------|
| Total absorbed enthalpy (kJ) | 14,776 | 11,701 | 8,434 |
| Total stored enthalpy (kJ) | 10,951 | 9,930 | 7,500 |
| Overall thermal efficiency (%) | 74.12 | 84.87 | 88.93 |

6. Conclusion and Discussion

According to the model validation result, the numerical model provides a reasonably accurate prediction of the thermal behavior and phase change characteristics of the eutectic alloy during charging and discharging cycles, with temperature trends and phase transition durations closely matching experimental data. Despite its simplified geometry, the model effectively illustrates the overall thermal response, although some aspects, like bidirectional heat extraction and thermal inertia, are excluded. These findings emphasize the importance of detailed boundary conditions and geometry, especially for systems involving complex heat transfer mechanisms.

The simulation results confirm that the oil domain exhibits turbulent flow, as validated by the Reynolds number, which is consistent with the assumptions of the k- ω SST turbulence model. The turbulent kinetic energy and intensity contours clearly demonstrate a shear-induced turbulence structure localized along the pipe walls, where high velocity gradients drive turbulent mixing and enhance convective heat transfer. This wall-bounded turbulence appears during both melting and solidification phases, but with reversed flow direction during solidification. However, minimal turbulence in the flow center is noticeable, unlike near the wall. Although the wall y^+ values do not fall within the optimal range for SST wall modeling, they remain within acceptable limits, balancing computational cost. Therefore, model optimization and a finer mesh can be done to tackle this problem. The model highlights the importance of boundary-layer dynamics in achieving effective heat transfer while simulating the TES.

The transient temperature profiles provide a comprehensive insight into the thermal response and heat distribution within the PCM during both charging and discharging cycles. The evolution of melting and solidification is well-captured by the thermocouples from inner to outer along the radial direction. During charging, the temperature plateau near 615 K confirms the eutectic temperature point and the dominance of latent heat absorption. It reflects a phase transition, which stabilizes after full melting when convective heat transfer becomes more significant in the liquid domain. Conversely, during discharging, a rapid temperature decline marks sensible cooling, followed by solidification that again occurs around the eutectic point, with the phase change propagating from bottom to top due to the reversed oil flow. The result demonstrates the eutectic alloy's thermal behavior and the effectiveness of the energy storage design in promoting consistent and directional heat transfer during both thermal cycles.

The analysis of melting and solidification times along the axial direction provides information that the discharging process is faster than the charging process. This phenomenon is probably due to internal heat transfer behavior with the effect of natural convection, rather than the temperature difference between the inlet and outlet of HTF. The time durations reflect heat propagation from the heated inner surface, with other surfaces assumed to be insulated. Although simulation captures the trend of faster solidification, validation conflicts remain when compared to experimental data, particularly due to geometric simplifications.

The combined analysis of charging and discharging processes demonstrates the distinct thermal behaviors governed by convection and conduction within the TES. During melting, strong natural convection enhances heat transfer from the heat source, leading to rapid and high fluid motion, especially when PCM is partially melted. In contrast, the solidification process is primarily conduction-dominated, with a more uniform downward thermal gradient and weaker convective activity due to reduced buoyancy forces in the cooled liquid. This results in a more symmetrical

phase front, consistent with the reversed HTF flow. The findings confirm that phase-change dynamics are strongly influenced by heat source positioning and flow direction, emphasizing the need for accurate modeling of thermal boundary conditions and buoyancy effects for both charging and discharging cycles in latent heat storage systems.

To advance the current study and improve the applicability of the model and materials, the following areas are proposed for future investigation:

- Incorporate detailed geometry according to the structural features of the experiment setup to more accurately simulate boundary conditions and capture bidirectional cooling effects during solidification.
- Adjust and validate key thermal parameters such as latent heat, specific heat, and thermal conductivity for improved agreement with experimental observations.
- Extend the simulation framework to study other eutectic and non-eutectic metal alloys, enabling selection or development of PCMs for specific applications.
- Modify other initial conditions, HTF inlet parameters, or domain orientation to examine how thermal behavior and phase front dynamics respond to different operating scenarios.
- Examine overall system efficiency, correlate with the power input to provide system optimization, and observe the efficiency over time
- Explore other computational models and calculations to come up with a better agreement when validating data and reflect more on the real thermophysical behavior of the eutectic alloy.
- Expand the model to account for long-term cycling, mechanical stress, or material degradation, offering the assessment of PCM reliability under real-world conditions.

References

- [1] Sarbu, I. and Sebarchievici, A., 2018. A comprehensive review of thermal energy storage. *Sustainability*, 10, p.191.
- [2] Prieto, C. and Cabeza, L.F., 2019. Thermal energy storage (TES) with phase change materials (PCM) in solar power plants (CSP): Concept and plant performance. *Applied Energy*, 254, p.113646.
- [3] Birchenall, C.E. and Riechman, A.F., 1980. Heat storage in eutectic alloys. *Metallurgical Transactions A*, 11A, pp.1415-1420.
- [4] Kenisarin, M.M., 2010. High-temperature phase change materials for thermal energy storage. *Renewable and Sustainable Energy Reviews*, 14, pp.950-970.
- [5] Aktay, K.S., Tamme, R. and Müller-Steinhagen, H., 2008. Thermal conductivity of high-temperature multicomponent materials with phase change. *International Journal of Thermophysics*, 29, pp.678-692.
- [6] Araki, N., Matsuura, M. and Makino, A., 1988. Measurement of thermophysical properties of molten salts: Mixtures of alkaline carbonate salts. *International Journal of Thermophysics*, 9, pp.1071-1080.
- [7] Farkas, D. and Birchenall, C.E., 1985. New eutectic alloys and their heats of transformation. *Metallurgical Transactions A*, 16A, pp.323-328.
- [8] Costa, S.C. and Kenisarin, M., 2022. A review of metallic materials for latent heat thermal energy storage: Thermophysical properties, applications, and challenges. *Renewable and Sustainable Energy Reviews*, 154, p.111812.
- [9] Bhattacharya, A., Kirna, A. and Karagadde, S., 2014. An enthalpy method for modeling eutectic solidification. *Computer Physics Communications*, 262, pp.217-230.
- [10] Gnauk, J., Wenke, R. and Frommeyer, G., 2005. Macroscopic modeling of solidification processes by performing the generalized enthalpy method. *Materials Science and Engineering: A*, 413-414, pp.490-496.
- [11] Li, Y., 2013. *Thermal performance analysis of a PCM combined solar chimney system for natural ventilation and heating/cooling*. PhD Thesis. Coventry University, UK.
- [12] Iten, M., Liu, S. and Shukla, A., 2018. Experimental validation of an air-PCM storage unit comparing the effective heat capacity and enthalpy methods through CFD simulations. *Energy*, 155, pp.495-503.
- [13] International Renewable Energy Agency (IRENA), 2013. *The Energy Technology Systems Analysis Programmes (ET SAP): Technology Brief E17*. Paris: International Energy Agency. Available at: <http://www.irena.org/Publications> [Accessed 15 Apr. 2025].
- [14] Kotzé, J.P., Theodor, W. and Erens, P.J., 2011. A combined latent thermal energy storage and steam generator concept using metallic phase change materials and metallic heat transfer fluids for concentrated solar power. *SolarPACES*.

- [15] Prieto, C., Cooper, P. and Fernández, I.A., 2016. Review of technology: Thermochemical energy storage for concentrated solar power plants. *Renewable and Sustainable Energy Reviews*, 60, pp.909-929.
- [16] Kumar, A. and Shukla, S.K., 2015. A review on thermal energy storage unit for solar thermal power plant application. *Energy Procedia*, 74, pp.462-469.
- [17] Murray, J.L. and McAlister, A.J., 1984. The Al-Si (Aluminum-Silicon) system. *National Bureau of Standards*, 5, pp.74-84.
- [18] Wang, X., Liu, J. and Zhang, Y., 2006. Experimental research on a kind of novel high temperature phase change storage heater. *Energy Conversion and Management*, 47, pp.2211-2222.
- [19] Blanco-Rodríguez, P., Rodríguez-Aseguinolaza, J. and Gil, A., 2015. Experiments on a lab-scale TES unit using eutectic metal alloy as PCM. *Energy Procedia*, 69, pp.769-778.
- [20] Risueno, E., Doppiu, S. and Rodríguez, A.J., 2016. Experimental investigation of Mg-Zn-Al metal alloys for latent heat storage application. *Journal of Alloys and Compounds*, 685, pp.724-732.
- [21] Mayer, S., Otic, I. and Cheng, X., 2016. Phase-field modeling of binary eutectic alloy solidification with convection. *Nuclear Science and Engineering*, 184, pp.377-387.
- [22] Jiménez-Xamán, C., Xamán, J. and Moraga, N.O., 2019. Solar chimneys with a phase change material for buildings: An overview using CFD and global energy balance. *Energy and Buildings*, 186, pp.384-404.
- [23] Blanco-Rodríguez, P. et al., 2014. Thermophysical characterization of Mg₅₁Zn eutectic metal alloy: A phase change material for thermal energy storage in direct steam generation applications. *Energy*, 72, pp.414-420.
- [24] Rodríguez-Aseguinolaza, J. et al., 2014. Thermodynamic study of the eutectic Mg₄₉-Zn₅₁ alloy used for thermal energy storage. *Journal of Thermal Analysis and Calorimetry*, 117, pp.93–99.
- [25] Zhou, J., Lehnhoff, T.F. and Tsai, H.L., 2006. Investigation of transport phenomena and defect formation in pulsed laser keyhole welding of zinc-coated steels. *Journal of Physics D: Applied Physics*, 39, p.5338.
- [26] The Dow Chemical Company, 2001. *Product Information: SYLTHERM 800*. 176-01469-1101 AMS, November 2001.
- [27] Brillo, J., Watanabe, M. and Fukuyama, H., 2021. Relation between excess volume, excess free energy and isothermal compressibility in liquid alloys. *Journal of Molecular Liquids*, 326, p.114395.
- [28] Battezzati, L. and Greer, A.L., 1989. The viscosity of liquid metals and alloys. *Acta Metallurgica*, 37, pp.1791-1802.

- [29] Kumar, S., Chaurasiya, V. and Singh, J., 2024. A computational study of binary eutectic system with convection under volumetric freezing: A moving boundary problem. *Thermal Science and Engineering Progress*, 50, p.102563.
- [30] Ao, X. et al., 2021. A numerical study of irregular eutectic in Al-Si alloys under a large undercooling. *Computational Materials Science*, 186, p.110049.
- [31] Kohlstadt, S., Vynnycky, M. and Goeke, S., 2021. On the CFD modelling of slamming of the metal melt in high-pressure die casting involving lost cores. *Metals*, 11, p.78.
- [32] Zappatore, A. et al., 2021. CFD analysis of natural convection cooling of the in-vessel components during a shutdown of the EU DEMO fusion reactor. *Fusion Engineering and Design*, 165, p.112252.
- [33] Shukla, P.K. and Kishan, P.A., 2019. CFD analysis of latent heat energy storage system with different geometric configurations and flow conditions. In: *Proc. 25th National and 3rd International ISHMT-ASTFE Heat and Mass Transfer Conference (IHMTC-2019)*, IIT Roorkee, India, Dec. 28–31.